MiniRetro: VLC Backscatter System for Miniaturized and Sustainable Internet of Things

JAVIER TALAVANTE, IMDEA Networks Institute, Spain and Universidad Carlos III de Madrid, Spain
BORJA GENOVES GUZMAN, Universidad Carlos III de Madrid, Spain
DOMENICO GIUSTINIANO, IMDEA Networks Institute, Spain

The proliferation of Internet of Things (IoT) devices demands communication technologies that are sustainable, low-power, and compact. While radio-frequency (RF) backscatter has enabled μW-level operation, its miniaturization is constrained by the physical limits of RF antennas. Visible light communication (VLC) backscatter offers an alternative by reusing existing lighting infrastructure, yet current designs require a significant area and power consumption at the IoT device. In this paper we present MiniRetro, a miniaturized VLC backscatter module with an active retroreflective area of only 0.25 cm^2, combining retroreflective sheetings with liquid crystal (LC) shutters. We model the VLC backscatter channel including the impact of retroreflector type, geometry, and photodiode (PD) placement, determining the configuration that maximizes the reflected signal strength. We also provide the first analytical and experimental framework characterizing the interaction between shutter and retroreflector, capturing polarization and transmittance losses and showing that the relative rotation angle can alter reflected power by up to 66%. We validate these features experimentally with a single-pixel VLC backscatter module, confirming a reliable meter-scale mobile communication while being the first VLC backscatter design to operate with a sub-cm^2 active area. Finally, we show its implementation on a small-sized aquatic robot providing uplink connectivity for aquaponics monitoring. Our results demonstrate the feasibility of MiniRetro as a miniaturized and sustainable VLC backscatter system for next-generation IoT connectivity.

CCS Concepts: • **Hardware** → **Wireless devices**; • **Networks** → **Physical links**.

Additional Key Words and Phrases: visible light communication, visible light backscatter, Internet of Things

ACM Reference Format:
Javier Talavante, Borja Genoves Guzman, and Domenico Giustiniano. 2026. *MiniRetro*: VLC Backscatter System for Miniaturized and Sustainable Internet of Things. *Proc. ACM Interact. Mob. Wearable Ubiquitous Technol.* 10, 4, Article 254 (December 2026), 28 pages. https://doi.org/10.1145/3857934

1 Introduction

The ever-increasing demand for Internet of Things (IoT) connectivity, together with its carbon footprint, calls for communication systems that are low-energy, compact, and sustainable. Meeting these requirements is challenging, especially when stringent cost and size constraints are present in emerging IoT applications.

To tackle this problem, backscatter communication has arisen as a proficient alternative, and has achieved attention both using ambient radio-frequency (RF) and visible light communication (VLC) technologies [22, 33]. RF backscatter leverages the availability of ambient RF signals to offload the generation of the RF carrier. While it offers μW-level operation, it faces miniaturization limits due to antenna constraints. According to Maxwell's equations, efficient radiation requires antenna lengths to be approximately half the signal wavelength ($\lambda/2$), creating a bottleneck for compact IoT transceivers.

Authors' Contact Information: Javier Talavante, jtalavan@pa.uc3m.es, IMDEA Networks Institute, Madrid, Spain and Universidad Carlos III de Madrid, Madrid, Spain; Borja Genoves Guzman, bgenoves@ing.uc3m.es, Universidad Carlos III de Madrid, Madrid, Spain; Domenico Giustiniano, domenico.giustiniano@networks.imdea.org, IMDEA Networks Institute, Madrid, Spain.

© 2026 Copyright held by the owner/author(s). Publication rights licensed to ACM.
This is the author's version of the work. It is posted here for your personal use. Not for redistribution. The definitive Version of Record was published in *Proceedings of the ACM on Interactive, Mobile, Wearable and Ubiquitous Technologies*, https://doi.org/10.1145/3857934.

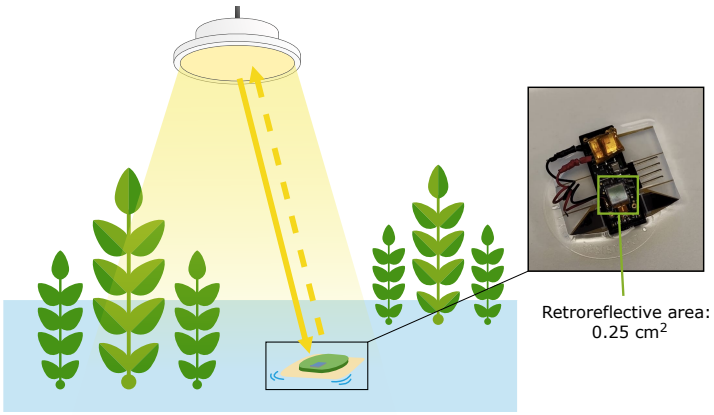


Fig. 1. Miniaturized VLC backscatter system for uplink in sustainable IoT use cases, such as aquaponics monitoring.

A backscatter transmission at 800 MHz, for instance, requires an antenna length of 18.7 cm, with printed circuit options using a radiating surface of hundreds of cm^2. Even at millimeter-wave frequencies, a half-wavelength element remains 2.5 mm long and typically needs arrayed structures for sufficient gain and directionality. Recent mm-wave backscatter systems such as mmTag [32] and Van Atta-array designs [20] still need footprints of 4.8–30 cm^2 to compensate for free-space loss and beam alignment. In contrast, computation follows Moore's law, continuously shrinking in size and power consumption.

This growing mismatch between communication and computation scaling motivates exploring alternative modalities that decouple device size from wavelength. Unlike RF antennas, VLC backscatter modules scale with area, not wavelength, overcoming the antenna-size limitations imposed by Maxwell's equations. In environments with lighting infrastructure, VLC backscatter has been demonstrated as a viable alternative for IoT applications [15, 53]. In VLC backscatter, the light-emitting diode (LED) source emits a light signal which is modulated by the IoT device and detected by a photodiode (PD) in proximity to the LED. The underlying principle is the use of reflective surfaces, such as retroreflectors, and low-power liquid crystal (LC) shutters. By opening and closing the shutter, the reflected light is modulated by the IoT device and sent back toward the source.

Despite this effort, current VLC backscatter designs do not fulfill key requirements for large-scale IoT deployment: small form-factor, low power consumption and low cost while achieving sufficient communication range. A key challenge is that LC shutter power consumption scales linearly with its area [41]. However, reducing the active area of the VLC backscatter module significantly lowers the reflected light power. Then, prior research has largely focused on VLC backscatter solutions with large form factors to ensure sufficient signal power and reliable communication performance [47]. However, such bulky designs remain impractical for the footprint constraints of modern IoT devices. This work aims to understand the dependency between device size and backscatter power by conducting a rigorous study of the optical channel model and optimizing the configuration of different elements.

This paper addresses the problem of optical efficiency of VLC backscatter systems for miniaturized, sustainable IoT with both theory and experiments. An illustration of the concept is shown in Fig. 1 for the use case of a tiny robot swimming on the surface of the water, operating with sub-centimeter-scale retroreflective surfaces and LC shutters. We achieve this by addressing two key challenges:

Design of the VLC backscatter system elements to maximize the uplink received optical power: building on prior VLC backscatter systems, we study the underexplored interaction of retroreflective sheetings

and LC shutters. Retroreflective-material characterization, while well-established for industrial and vehicular applications, remains underexplored in wireless communication systems.

Modeling the retroreflector-LC shutter impacts on communications: the LC shutter and retroreflective sheeting jointly produce optical effects such as polarization and reflection that, when both elements are combined for VLC backscatter, dramatically affect the reflected optical power.

To address these challenges, we present our core contributions below. These consist of two primary theoretical insights, followed by two engineering contributions that empirically validate our findings:

- **VLC backscatter geometry optimization**: Prior works did not study the interaction between elements of the VLC backscatter system. We here demonstrate that their configuration has a dramatic impact on communication. In this work, we analyse the properties of retroreflective sheetings from their industrial-environment characterization, deriving the optimal sheeting type and element placement to maximize the optical reflected power.
- **Characterization of the LC shutter-retroreflector interaction**: We provide an analytical and experimental framework to maximize the optical power reflected by a retroreflector-LC shutter element in IoT devices. For the first time, we study the effect of LC shutter rotation over the retroreflective sheeting and identify orientations that increase the reflected power by up to 66%.
- **Implementation and evaluation of a miniaturized VLC backscatter module**: We prototype and evaluate MiniRetro, a single-pixel LC shutter retroreflector module with an active area of 0.25 cm^2, *the smallest VLC backscatter design to date*; two orders of magnitude smaller than typical mm-wave backscatter tags and several orders of magnitude smaller than backscatter in the traditional 800 MHz band. MiniRetro maintains reliable communication at hundreds of Hz and meter-scale indoor range.
- **Real use case study**: We deploy and test our system on a small-sized aquatic robot, demonstrating reliable uplink communication for aquaponics monitoring. It maintains the connectivity despite surface disturbances and water reflections, while satisfying the power budget of such devices. We further demonstrate a multi-node deployment, coordinating access across multiple robots via a VLC downlink and time division, and discuss additional application scenarios enabled by miniaturization, including consumer tracking, biomedical asset monitoring, and RF-free medical sensing. We provide a supplementary video of the system operating on an aquatic robot.

The rest of the paper is structured as follows: We first introduce the works related to this paper in Section 2. In Section 3 we provide an overview of the VLC backscatter communication used in this study. Section 4 derives the communication channel model while introducing specific properties of the devices in the system. Section 5 validates the theory derived in Section 4. In Section 6, we present the simulation results showing the impact of the properties analyzed before. Section 7 shows the implementation and experimental results of MiniRetro. We then demonstrate its performance in an aquaponics application in Section 8, while detailing further applications in Section 9. We finally present the system limitations in Section 10 and conclude the paper in Section 11.

We release MiniRetro's hardware and software code used in the real case study as open source, to facilitate reproducibility and foster further research in the community[1].

2 Related Work

RF backscatter systems. Reusing RF radiation to perform RF backscatter enables power consumption in the order of μW [56] [11], which may even eliminate the need for batteries in IoT devices, reducing the carbon footprint of the communication technology [33]. However, RF backscatter relies heavily on antenna design, since

[1]The hardware and software designs used in this article can be found at: https://doi.org/10.5281/zenodo.22919131. A video demo can be found here: https://youtu.be/XNNPDoiPu5I.

Work	FoV [°]	Data rate[2]	Background light[3]	Active area [cm^2]	Distance [m]	FOM [m/(cm^2 · W)]
RetroVLC [25]	15	500 bps	300 lux	14.2	1.5	$59 \cdot 10^{-3}$
PassiveVLC [53]	4	1 kbps	2 klux	14.2	2.5	$9 \cdot 10^{-3}$
RetroI2V [47]	30	1 kbps	10 klux	3000	90	$1 \cdot 10^{-3}$
DroneVLC [13]	35.5	120 bps	2 klux	2×24.6	1.1	$45 \cdot 10^{-3}$
[39]	-	100 bps	<100 lux	12.96	5	$11 \cdot 10^{-3}$
RetroTurbo [49]	20	8 kbps	1 klux	66	12	$45 \cdot 10^{-3}$
Pixelated-VLC [38]	-	600 bps	300 lux	3×3.14	2	$25 \cdot 10^{-3}$
[48]	-	4 kbps	1 klux	16×10.2	6	$3 \cdot 10^{-3}$
RetroMUMIMO [51]	20	8×500 bps	1 klux	4×15	2.5	$10 \cdot 10^{-3}$
MiniRetro	30	200 bps	15 klux	0.25	3	$353 \cdot 10^{-3}$

Table 1. Comparison with VLC backscatter state-of-the-art.

the rest of the circuitry should be mostly passive. This imposes a relevant limitation on miniaturization and weight reduction of the IoT device, restraining the technology from being applied in specific scenarios.

Recent mm-Wave backscatter systems, including mmTag [32], MilBack [30], and mmComb [10], highlight the potential of mm-Wave frequencies but rely on centimeter-scale antenna or Van Atta array structures [20] to overcome free-space loss and achieve sufficient radar cross-section. Some RF backscatter systems instead reuse carrier signals from standards such as WiFi [55]. But most require an ad-hoc carrier generator dedicated to this task, particularly at higher radio frequencies, increasing system cost and deployment complexity. Finally, the relatively weak signal compared to active RF sources implies that 1) RF backscatter is vulnerable to interference in congested frequency bands [17], and 2) certain environments, such as aqueous media [36] or metallic structures [57] hinder its deployment. VLC backscatter tackles both issues thanks to the uncrowded nature of the visible-light spectrum and its strongly directional link.

VLC backscatter systems. Although VLC backscatter applied to IoT is a recent field, several experimental works have pushed forward the possibilities of these systems [45]. VLC allows illuminating and communicating simultaneously, making it practical where illumination is already required. We narrow the scope of our study to works suitable for miniaturization, using artificial light and enabling high mobility. Table 1 compares VLC backscatter works for IoT fitting these requirements.

This excludes two families of works out of scope for our study. First, those using ambient light for communication [6, 15]: sunlight acts as the carrier, removing the need for an LED, but deployment then depends on sunlight conditions and indoor layout. Second, works using highly directive, reflectable sources such as lasers, which require steering mechanisms typical IoT devices cannot support [7–9].

RetroVLC [25] is the first work applying VLC backscatter to battery-free devices, implementing a bidirectional system with VLC for downlink and VLC backscatter for uplink on a credit-card-sized tag, with the area dedicated to VLC backscatter being 14.2 cm^2. PassiveVLC [53] extended this with a modulation adapted to the limitations of the LC shutter, achieving 1 kbps. VLC backscatter is not exclusive to small-sized devices, as shown in RetroI2V [47], which uses retroreflective traffic signs as VLC backscatter modulators, whose large area enables vehicle-to-infrastructure communication up to 90 m. DroneVLC [13] implements the concept in battery-free drones, using a low-power LED. Authors in [39] extend the battery-free range to 5 m in tunneled environments.

[2]Maximum reported in most beneficial circumstances.
[3]Maximum reported.

Recent studies exploit LC shutter optics for tailored encoding schemes and modulations: RetroTurbo [49] rotates shutters to separate signals by polarization for quadrature modulation. Also, receiver-side polarizers can filter noise [48], improving data rate at the cost of mobility, since the IoT device cannot rotate; Pixelated-VLC [38] explores modulations based on multiple small shutters. Finally, RetroMUMIMO [51] achieves concurrent transmissions via pulse feature extraction.

A common thread across these systems is that performance is fundamentally tied to the size of the reflecting element. In VLC backscatter, the reflected optical power scales with the active area of the retroreflector, so achieving longer communication range has so far required progressively larger backscatter modules. This trend is evident in Table 1, where the longest-range designs also exhibit the largest active areas. Such a dependency constrains the practical deployment of VLC backscatter in size-limited IoT devices. In contrast, this work studies the regime in which the active area of the reflecting element is constrained to a sub-cm^2 scale, examining the range and reliability attainable in this context.

For a better understanding of this trade-off, we define a figure of merit (FOM) that jointly captures the relationship between the achieved distance ($d_{\max}$), the active retroreflective area (A_R) and the optical transmit power of the artificial light source (P_{opt}):

$$\text{FOM} = \frac{d_{\max}}{A_R \cdot P_{\text{opt}}}. \tag{1}$$

This metric normalizes performance by device size and illumination power, enabling fair comparison across heterogeneous designs. As both A_R and P_{opt} increase the reflected power into the PD, a larger FOM indicates better link efficiency with respect to those two parameters. Table 1 summarizes this FOM for state-of-the-art VLC backscatter systems and our proposed system; MiniRetro achieves a FOM 6× higher than the closest prior design, highlighting its superior joint efficiency in area, range, and power.

Other factors also determine the performance of the deployment. Several works increase the data rate of VLC backscatter through more complex modulations compensating LC shutter limitations [49] or multiple modulating elements [51]. Many of these techniques can be extrapolated to miniaturized designs, but they are limited by device availability at this scale. Background light is another limitation, given PD saturation under strong ambient light [21]. While a unified benchmark capturing all these factors remains an open challenge, the introduced FOM provides a first step toward fair comparison along the most critical dimensions for miniaturization.

3 System Overview and Design Motivation

MiniRetro aims to enable VLC backscatter in miniaturized, low-power IoT devices. As shown in Fig. 2, a VLC backscatter link uses an optical transceiver that integrates an LED source and a PD to detect the modulated reflections returned by the IoT device, which relies on a miniaturized VLC backscatter module encoding data by modulating the incident illumination. LED lighting can also provide conventional VLC in the downlink.

Designing such a system requires balancing three conflicting aspects: device size, reflected signal strength, and power consumption. Since both the reflected optical power and the LC shutter's energy consumption scale linearly with active optical area, reliable communication at sub-centimeter scale imposes stringent design constraints.

To guide our design, we define the following practical requirements for a miniaturized VLC backscatter system:

- **Low power consumption:** The total power budget must remain in the order of a few μW, allowing battery-free or energy-harvested operation.
- **Compact form factor:** The active optical area must be smaller than 1 cm^2 to enable integration in small IoT nodes such as wearable or robotic platforms.
- **Adequate communication performance:** The system must sustain reliable backscatter at distances up to a few meters for data rates of tens to hundreds of bps, sufficient for low-rate sensing and telemetry, while remaining robust to strong background illumination.

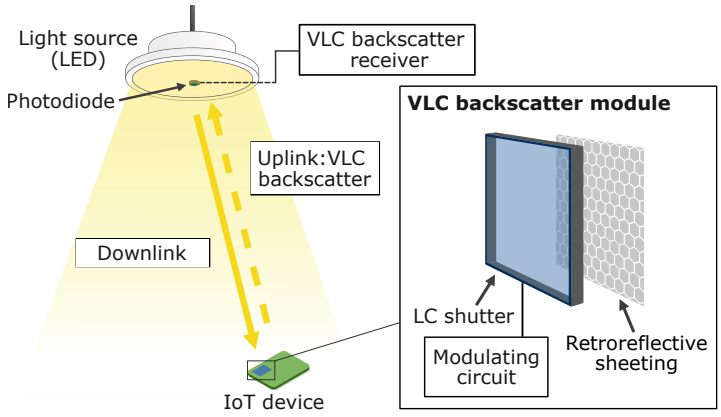
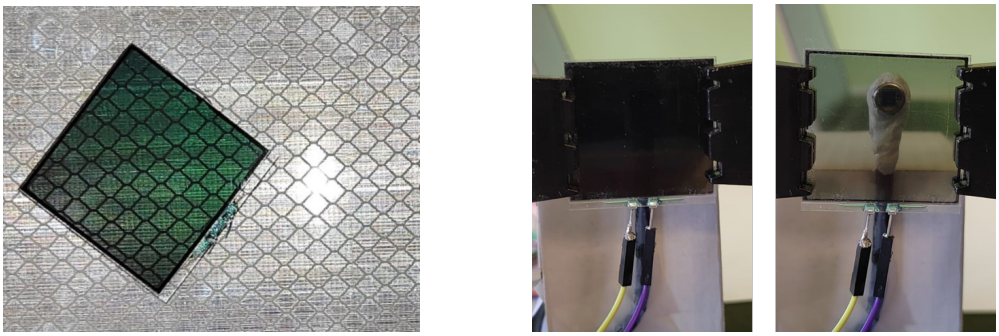


Fig. 2. Overview of the VLC backscatter system under study.



(a) LC Shutter and retroreflector effect on the flash of a camera.

(b) LC shutter and its light modulating effect, in open and closed states.

Fig. 3. Samples of a retroreflective sheeting (3M™ DG 4090) and LC shutter with its modulating driver.

- **Low cost and material simplicity:** The components must be made of inexpensive, mass-produced materials such as polymer films and liquid crystals. The overall cost per tag should remain in the range of a few euros, enabling scalable deployments.

These requirements form the foundation for the system architecture of MiniRetro. Next, we describe the key components of the IoT VLC backscatter module.

3.1 IoT VLC Backscatter Module

The IoT module of MiniRetro modulates incident light by combining two optical elements: a retroreflective sheeting and an LC shutter.

Retroreflective sheeting: This element reflects light impinging onto its surface back in the direction it arrived from. It is formed by microscopic corner-cube structures known as single-block corner-cube retroreflectors [53]. Owing to their low cost, thin profile, and ease of integration, retroreflective sheetings are the most practical choice for IoT applications. Fig. 3a shows the visual appearance of the sheeting. We observe a region where *more light is reflected from the flash into the camera sensor*. Understanding the efficiency of retroreflection with respect

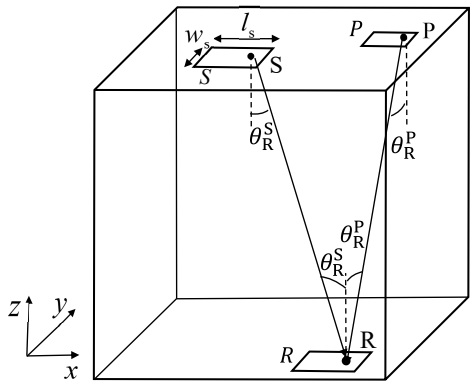


Fig. 4. System model including a light source (S), a retroreflector sheeting (R) and a photodetector (P).

to the relative position of the light source, retroreflector and detector is therefore key to optimizing the VLC backscatter performance.

LC shutter and its modulating circuit: This element allows passing or blocking light depending on the voltage applied by the modulating driver. An LC shutter consists of an LC layer between two electrodes and two polarized layers in perpendicular directions. A voltage difference between terminals aligns the LC molecules, rotating the polarization of light from the first polarizer by 90° and blocking it in the second one. Controlling this voltage modulates the transmitted light fast enough to transmit data. Fig. 3b shows the shutter in open and closed modes. In the simplest scheme, applying voltage encodes bit '0', while no voltage opens the shutter for bit '1'.

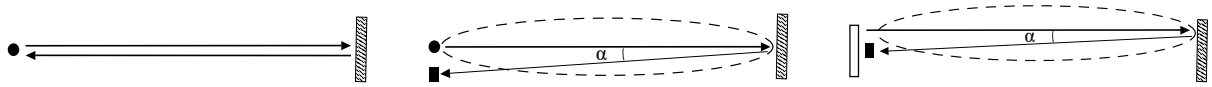
Summary

A detailed understanding of the dependency between the incident illumination pattern, the retroreflector's angular response, and the optical behavior of the shutter is necessary to inform both the physical design of the module and the LED-PD placement of system components. To that end, we next formulate an analytical model of the VLC backscatter channel that captures geometric propagation losses as well as the device-specific phenomena introduced by the LC shutter and retroreflective sheeting. This model provides the basis for the design insights and system optimization presented in the following sections.

4 Backscattered Optical Channel Model

To guide the design of MiniRetro and understand which parameters fundamentally limit miniaturization, we require a channel model capturing both geometric propagation losses and device-specific optical phenomena. We formulate that model by decomposing the backscatter link into the light source-to-retroreflector path (Section 4.1), the retroreflector-to-photodetector return (Section 4.2), and the LC-shutter–induced polarization and transmittance losses (Section 4.3), seeking to minimize power losses and improve communication performance.

System model. From the scenario in Fig. 2, we derive three elements in the VLC backscatter system: light source, retroreflector and photodetector, represented by the sets of points S, R and P, respectively. Fig. 4 shows a diagram of the system model including these elements. The light source is ceiling-mounted on the horizontal x-y plane, providing both illumination and VLC backscatter communication. The VLC backscatter module containing the retroreflector is located around the room pointing upwards. The photodetector is on the same horizontal plane as the source.



(a) Perfect retroreflector. (b) Imperfect retroreflector. (c) Extended source of light with an imperfect retroreflector.

Fig. 5. Possible configurations of the three elements of the VLC backscatter link: light source, retroreflector and photodetector.

The proposed backscattered optical channel H is composed by three different contributions, formulated by:

$$H = H_{S,R} \cdot H_{R,P} \cdot H_{LC}, \tag{2}$$

where $H_{S,R}$ accounts for the free-space path loss from the source to the whole retroreflector surface, $H_{R,P}$ considers the free-space path loss from the retroreflector to the photodetector, and H_{LC} models the losses inherent to using the LC shutter-retroreflector combination for modulating data, which are independent of the spatial disposition of S, R and P.

4.1 Optical Source-to-Retroreflector Channel

Let us name $P_{\mathrm{R}}^{\mathrm{S}}$ as the optical power arriving at a point $\mathrm{R} \in R$ coming from a point $\mathrm{S} \in S$. Assuming that all source points emit as a Lambertian source:

$$P_{\mathrm{R}}^{\mathrm{S}} = \frac{P_{\mathrm{opt,S}} \cdot (m+1) \cdot \cos^m(\theta_{\mathrm{R}}^{\mathrm{S}}) \cdot \mathrm{d}A_R}{2\pi D_{\mathrm{S,R}}^2}, \tag{3}$$

where $P_{\mathrm{opt,S}}$ is the emitted power from S. We assume that the light source has a uniform power distribution along its area $A_S = w_s \cdot l_s$, and then $P_{\mathrm{opt,S}} = (P_{\mathrm{opt}} \cdot \mathrm{d}A_S)/A_S$, where P_{opt} is the total transmit optical power and $\mathrm{d}A_S$ is the infinitesimally small area of S. $\theta_{\mathrm{R}}^{\mathrm{S}}$ is the angle created by the vector connecting points S and R and the optical axis of the source S that is normal to the source, retroreflector and photodetector surfaces, while $D_{\mathrm{S,R}}$ is the Euclidean distance between points S and R. The Lambertian index, m, determined by the LED's half-power semi-angle $\phi_{1/2}$, is $m = -1/\log_2\left(\cos\left(\phi_{1/2}\right)\right)$.

Considering a retroreflector with area A_R, we can formulate $H_{S,R}$ accounting for all source and retroreflector points as

$$H_{S,R} = \frac{P_R^S}{P_{\mathrm{opt}}} = \frac{m+1}{2\pi A_S} \int_{A_R} \int_{A_S} \frac{\cos^m(\theta_{\mathrm{R}}^{\mathrm{S}})}{D_{\mathrm{S,R}}^2} \cdot \mathrm{d}A_S \mathrm{d}A_R, \tag{4}$$

where P_R^S is the total power received at the retroreflector area R emitted from the source S.

4.2 Optical Retroreflector-to-Photodetector Channel

We now compute how much light is reflected back to the detector. First, we must outline the key properties of the retroreflective sheeting used in our design.

- **Ideal retroreflection is unusable for VLC backscatter.** An ideal retroreflector sends light back exactly along its incident direction (Fig. 5a). In a VLC backscatter link, this would prevent the modulated light from reaching the PD, since the return beam would either follow the LED's emission axis and miss the PD, or be blocked by the LED itself.
- **Real retroreflective sheetings behave as imperfect retroreflectors.** Commercial sheetings deviate slightly from perfect retroreflection and scatter part of the incoming light within a small angular cone (Fig. 5b). This non-ideal behavior enables a detectable return signal.

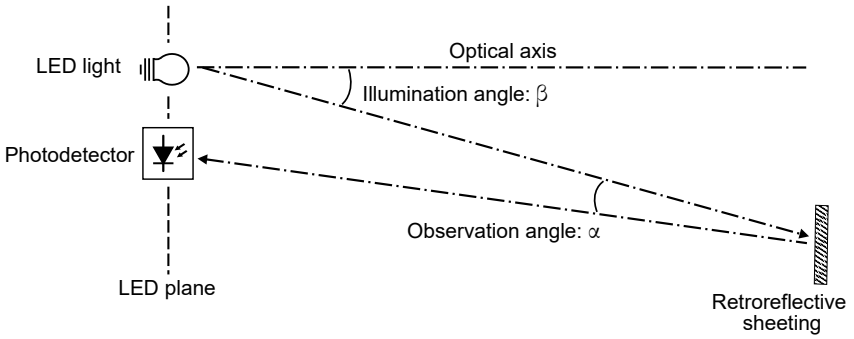


Fig. 6. Disposition of the LED, retroreflector and receiver in the VLC backscatter link, where angles α and β determine R_A.

- **The *observation angle* α governs the reflected intensity.** The angle between the incoming ray and the dominant reflected direction, denoted by α, determines the efficiency of the retroreflection. Since α depends on the relative placement of the LED and PD, it becomes a central geometric parameter in our model.
- **Practical VLC backscatter arises from extended emitters and nearby detectors.** When using an LED with a diffuser (large emitting area) and a small photodetector placed near it, the resulting observation angle α falls within the high-efficiency region of the sheeting (Fig. 5c). This configuration enables a practical backscatter link with industrial retroreflective materials.

The intensity of the reflected signal is captured by the *retroreflection coefficient* R_A, which measures *how efficiently the sheeting concentrates incident light back toward the light source plane*. Formally,

$$R_A = \frac{I}{\Phi_\mathrm{V}} \quad \left[\frac{\mathrm{cd}}{\mathrm{lm}} = \mathrm{sr}^{-1}\right], \tag{5}$$

where I is the reflected luminous intensity and Φ_V is the incident luminous flux on the retroreflective surface.

4.2.1 Dependence on α and β. R_A measurement is regulated by standards [4] and is highly sensitive to α. In our setting *moving the photodetector along the LED plane directly changes α* (Fig. 6); even centimeter-scale shifts can substantially reduce R_A, making LED-PD placement a fundamental design consideration.

R_A also depends on the *illumination angle* β, the angle between the LED optical axis and the ray incident on the retroreflector (Fig. 6). Shifting the module laterally modifies β, and higher β values reduce R_A due to reduced effective area and absorption in the sheeting's protective layers. Together, $R_A(\alpha, \beta)$ determines how much modulated light re-enters the LED plane.

4.2.2 Computation of channel model. As expressed in Eq. (5), R_A is measured in sr^{-1}; we convert it to a unitless gain in optical received power by multiplying it by the solid angle occupied by the receiver. Since α and β differ for every combination of S, R and P points, we use the notation $R_{A,\mathrm{S-R-P}}$ to denote R_A for such points.

We define P_P^R as the power arriving at a point P $\in P$ coming from a point R$\in R$, formulated as

$$P_\mathrm{P}^\mathrm{R} = \mathrm{d}P_\mathrm{R}^S \frac{\mathrm{d}A_P}{D_\mathrm{R,P}^2} \cdot R_{A,\mathrm{S-R-P}}, \tag{6}$$

where $\mathrm{d}P_\mathrm{R}^S$ is the power that arrives from S to the point P, $\mathrm{d}A_P$ is an infinitesimally small area of the photodetector surface and $D_\mathrm{R,P}$ is the Euclidean distance between the points R and P. Since $\mathrm{d}A_P \ll D_\mathrm{R,P}^2$, dividing the area of the photodetector P ensures that the calculation of the solid angle is sufficiently precise.

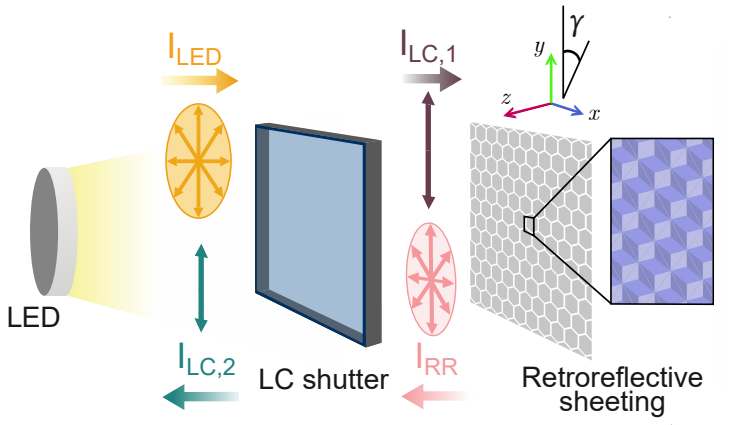


Fig. 7. Representation of how light travels through the LC shutter and retroreflector. We also represent how the modification of the light polarization is produced by the VLC backscatter module.

Since R_A already accounts for retroreflector inclination, no projection factor $\cos(\theta_{\mathrm{R}}^{\mathrm{S}})$ is required. Therefore, $H_{R,P}$ can be written as the ratio between the total power received in the photodetector area P reflected from the retroreflector R, denoted by P_P^R, and the total power received in the retroreflector area R emitted from the source S, denoted by P_R^S:

$$H_{R,P} = \frac{P_P^R}{P_R^S} = \int_{A_P}\int_{A_R} \frac{P_{\mathrm{R}}^{\mathrm{S}}}{D_{\mathrm{R,P}}^2} \cdot R_{A,\mathrm{S-R-P}} \cdot \mathrm{d}A_R \mathrm{d}A_P. \tag{7}$$

4.3 LC Shutter-Retroreflector Losses

An LC shutter comprises two linear polarizers with orthogonal polarization directions placed on each side of the LC cell. When unpolarized light arrives at the first polarizer, only light in its polarization direction enters the LC cell. Depending on the voltage between its terminals, this cell can rotate 90° the polarization of the incoming light. If this is performed, the second polarizer, commonly known as the analyzer, allows light to come out of the LC shutter (open state). Otherwise, the analyzer blocks it (closed state) [49].

The LC shutter introduces several optical losses that determine how much modulated light exits the module and reaches the photodetector. To capture these effects in the channel model, we decompose the shutter-induced attenuation into two main contributions:

- **Polarization loss** ($\overline{\rho}_{pol}$), caused by the LC shutter acting as a polarization filter twice (see Fig. 7).
- **Transmittance loss** ($\overline{\rho}_{\mathrm{trans}}$), caused by absorption in the LC material and its polarizer layers.

We incorporate both effects through the LC loss term:

$$H_{LC} = \overline{\rho}_{pol} \cdot \overline{\rho}_{\mathrm{trans}}. \tag{8}$$

A key characteristic of the system is that the light: (i) passes through the LC shutter, (ii) is retroreflected, where its polarization may change, and (iii) passes through the LC shutter again. This interaction, illustrated in Fig. 7, produces nontrivial losses that we model below.

4.3.1 Polarization loss ($\overline{\rho}_{pol}$). Fig. 7 shows the polarization at each stage of the path along the LC shutter and retroreflective sheeting. Considering the light passing through the shutter twice, we can define the loss produced

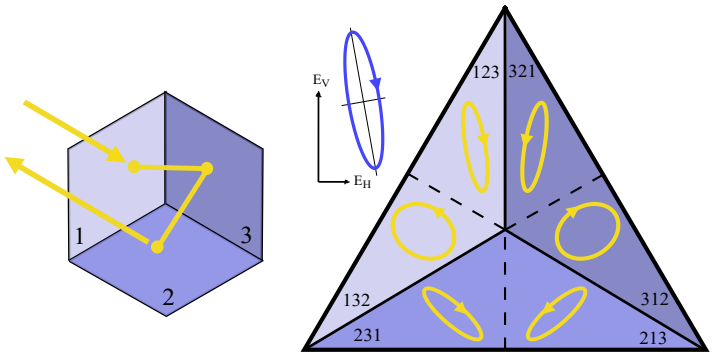


Fig. 8. Light reflection on a corner-cube retroreflector and output polarization for a vertically polarized input. This depends on the order in which light hits the three sides of the cube (left) and is determined by the first region *abc* onto which the light impinges (right).

by the polarization filtering on the LC shutter as:

$$\overline{\rho}_{\text{pol}} = \rho_{\text{pol},1} \cdot \rho_{\text{pol},2}, \tag{9}$$

where $\rho_{\text{pol},1}$ and $\rho_{\text{pol},2}$ are the power losses produced the first time and the second time the light passes through the LC shutter, respectively. When unpolarized light reaches the entrance polarizer, only one polarization component is transmitted, i.e., $\rho_{\text{pol},1} = 0.5$.

Then, the retroreflected light I_{RR} passes through the shutter again, leading to $I_{\text{LC},2}$ that is directed to the photodetector. If the retroreflective sheeting preserves the polarization of light, zero light would be blocked by the LC shutter, resulting in $\rho_{\text{pol},2} = 1$. However, the retroreflective sheeting modifies the polarization of the returned light, a behavior often neglected in prior models, due to the microscopic structure of the corner-cube array.

The best-performing retroreflective sheeting is usually composed of an array of microscopic reflective corner-cubes or trihedrons [29]. As shown in Fig. 8, light impinges on one side, reflects off the other two, and returns to the source. Single-block corner-cube retroreflectors used in precision optics may alter polarization [44]. Therefore, a sheeting built from miniaturized analogous structures can do so as well.

Corner-cube retroreflectors can operate via specular reflection or total internal reflection (TIR). Specular reflection, produced by a very smooth, highly reflective surface, is used in high-end retroreflectors and preserves the incoming polarization of the incoming ray. On the contrary, in TIR-based retroreflectors, the difference between refractive indices of the materials produces the reflection and, due to the actual change of medium and direction, they tend to modify the polarization [44]. Retroreflective sheeting is usually TIR-based [54], since specular retroreflectors require more expensive processes and materials.

Fig. 8 shows how the corner-cube retroreflector changes the polarization of vertically polarized light (E_v). The active area of the corner-cube is divided into six regions depending on the order of the surfaces (1, 2 and 3) on which the light bounces. Each region produces a different elliptical polarization output. We can represent this change by defining the Jones matrix J_{abc} of each region [27], where the subindex *abc* indicates the order in which light hits the three sides and is reflected back. The Jones matrices for each region and the derivation of the power loss produced the second time the light passes through the LC shutter $\rho_{\text{pol},2}$ are described in the Appendix.

4.3.2 Transmittance loss ($\overline{\rho}_{\text{trans}}$). In addition to polarization filtering, the LC shutter attenuates light due to absorption in the LC layer and polarizers. Assuming that the spectral flux of the incoming light $\Phi_V(\lambda)$ emitted by

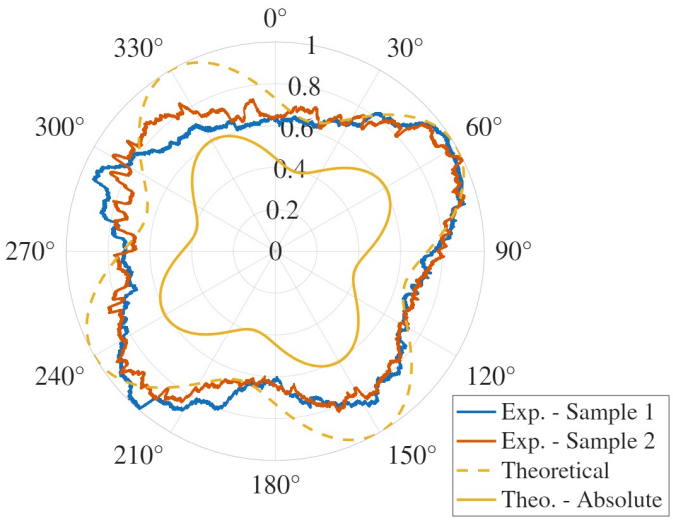


Fig. 9. Comparison of experimental and theoretical relative returned optical power from the VLC backscatter module with respect to angle γ.

the source is known, we can define the effective transmittance $\overline{\rho}_{\text{trans}}$ as

$$\overline{\rho}_{\text{trans}} = \frac{\int_{-\infty}^{\infty} \Phi_V(\lambda)\, T^2(\lambda)\, d\lambda}{\int_{-\infty}^{\infty} \Phi_V(\lambda)\, d\lambda}, \tag{10}$$

where $T(\lambda)$ is the spectral transmittance of the LC shutter. Note that $T(\lambda)$ appears to the power of two as the light in the VLC backscatter system passes through the LC shutter twice.

Summary and Key Insights

This analysis yields two findings, later confirmed experimentally and guiding the design of MiniRetro. First, the LC shutter-retroreflector interaction impacts the total reflected power. The relative rotation angle between the two elements modifies the reflected intensity, as we validate in Section 5, highlighting the need for careful mechanical alignment in miniaturized VLC backscatter modules.

Second, transmitter-receiver geometry strongly affects link efficiency. Specifically, placing the PD at the LED center maximizes received signal-to-noise ratio (SNR) by minimizing the observation angle and exploiting the retroreflector's peak-efficiency region. We confirm this insight through simulation and experimental results in Sections 6 and 7.

5 Experimental Analysis of Polarization Losses

In this section we experimentally validate the novel theoretical analysis developed in Section 4. Note that transmittance losses produced by the LC shutter are not analyzed here, as it is a well-studied effect.

We aim to confirm the power loss produced by the polarization in an LC shutter, deploying an experimental setup replicating Fig. 7. We use a 3M retroreflector sheeting DG 4090 (Fig. 3a), testing two samples for reliability. We place the sheeting behind the shutter, and illuminate both of them with an LED. Then, we rotate the sheeting coaxially with the static shutter to emulate all γ angles, measuring reflected power with a PD in front of the LED.

We set $\gamma = 0°$ as the orientation placing the straight-line pattern of the sheeting vertically. This is the orientation recommended by the manufacturer for general use, but not optimal for VLC backscatter, as shown below.

Fig. 9 shows both the theoretical and experimental results. We show the normalized optical power measured for each sample with respect to γ (blue, red). We normalize the measurements to remove effects our setup cannot isolate, such as the shutter transmittance loss. We also plot the theoretical intensity exiting the shutter, $I_{\mathrm{LC},2}(\gamma)$, calculated from (15) (yellow solid), and its normalized version for comparison with experimental data (yellow dashed). Both theoretical and experimental results form a four-lobe structure, separated from each other by 90°.

Choosing a wrong γ can theoretically lead to a loss of up to 56% of the optical power. Ensuring proper LC shutter-retroreflector orientation is therefore important, and is a simple adjustment to make on the module. In particular, we find that the best experimental response is obtained at $\gamma = 60°$ for this combination of LC shutter and retroreflective sheeting, achieving a gain of 66% with respect to $\gamma = 0°$, as recommended by the manufacturer. The mismatch with theory stems from assuming a perfect corner-cube matrix, which manufacturers need not maintain. Finally, the theoretical absolute polarization loss, equivalent to $\rho_{\mathrm{pol},2}(\gamma)$, equals 0.61 with the best alignment possible. This means that this type of device incurs a power loss greater than the one typically expected due to polarization after being reflected.

6 Simulation-Driven Insights Into the VLC Backscatter Channel

Let us now analyze the performance of the proposed VLC backscatter channel for different configuration parameters. We assume an LED source and a PD on the ceiling, with the optical power emitted by the LED being modulated and backscattered by the retroreflector before reaching the PD. The electrical SNR at the PD can be calculated as

$$\mathrm{SNR} = \frac{(P_{\mathrm{opt}} \cdot H \cdot \eta)^2}{N_0 \cdot B}, \tag{11}$$

where P_{opt} is the optical power emitted by the LED, H is the total backscattered optical channel proposed in Eq. (2), η is the responsivity of the photodetector in A/W, N_0 is the noise spectral density and B is the system bandwidth. The product $P_{\mathrm{opt}} \cdot H \cdot \eta$ contributes linearly to the received current but quadratically to the electrical SNR, since the photodiode converts incident optical power into electrical current.

The simulation parameters are summarized in Table 2. They were selected considering an implementation with standard devices. We assume the LC shutter produces a severe 50% power loss ($\rho_{\mathrm{pol},1} = 0.5$) the first time unpolarized light passes through it, and a more relaxed 39% loss ($\rho_{\mathrm{pol},2} = 0.61$) the second time. We further consider a reasonable value of 42% as transmittance loss ($\overline{\rho}_{\mathrm{trans}} = 0.58$).

Fig. 10 shows the retroreflection coefficient R_A for different types of retroreflective sheeting, as classified by the standard ASTM 4956-19 [5], which establishes minimum R_A for standard values of $\alpha \in [0.2°, 0.5°, 1°]$ and $\beta \in [4°, 30°]$. We consider white retroreflectors, as they are more common and maximize reflected power for white LEDs, commonly used for illumination.

We can also see that $\alpha = 1°$ is defined by the standard only for Types IX and XI, as this observation angle may not be encountered in certain scenarios. In the VLC backscatter case, this means these types are more effective when leveraging the light from diffuse sources: the light from the LED borders (high α) will still be reflected to the PD. We accordingly define Types IX and XI as *diffuse*, and the rest as *directive*.

Vertical separation. Fig. 11 shows the SNR received by the PD for different vertical distances. We assume a Type XI retroreflector, interpolating R_A from the nearest tabulated values near $\alpha = \beta = 0°$, where it is undefined. As expected, SNR decreases with distance, and larger A_R yields higher link margin. For indoor separations up to around 2 m, retroreflector areas above 1 cm^2 provide sufficient SNR for reliable communication.

This threshold corresponds to electrical SNR at the PD output. In practice, our prototype (Section 7) employs practical amplifiers and envelope detection, which mitigate wideband noise and recover the modulated backscatter

Parameter	Description	Value
P_{opt}	Optical LED transmit power	40 W
$\phi_{1/2}$	LED's half-power semi-angle	60°
w_s	Source width	10 cm
l_s	Source length	10 cm
A_P	Photodetector area	1 cm^2
-	Vertical LED-RR distance	[0.5 - 3] m
$\rho_{\text{pol},1}$	Polarization power loss (1^{st})	0.5
$\rho_{\text{pol},2}$	Polarization power loss (2^{nd})	0.61
$\overline{\rho}_{\text{trans}}$	Transmittance power loss	0.58
η	Photodetector responsivity (white)	0.4 A/W [35]
N_0	Noise power spectral density	$2.5 \cdot 10^{-17}$ A^2/Hz
B	Bandwidth	1 kHz

Table 2. Simulation parameters.

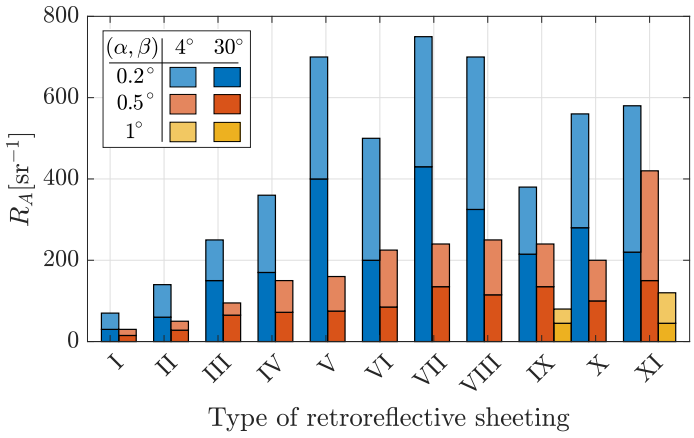


Fig. 10. R_A for different types of retroreflectors [5] for the reference values of α (column) and β (row).

signal with significantly lower instantaneous SNR. These implementation-level processing gains allow our system in Sections 7 and 8 to operate reliably with smaller retroreflector areas of 0.25 cm^2.

Horizontal displacement and PD placement. Fig. 12 analyzes the SNR as the retroreflector moves horizontally at a fixed 1 m vertical separation. The plot shows how SNR drops as the Euclidean distance increases and the retroreflection coefficient decreases. Also, regarding the position of the PD relative to the LED, we observe maximum SNR when the PD is centered; even a 10 cm displacement reduces SNR by roughly 20 dB for a Type XI retroreflector. This highlights that optimal PD placement is critical since it strongly affects α.

Retroreflector type comparison. Fig. 12 also compares the most directive retroreflector (Type VII) against two diffuse ones (Type IX and XI). Although Type VII offers the highest retroreflection coefficient at low α and β (Fig. 10), this does not translate into better performance. Most of the reflecting area of the retroreflector sees

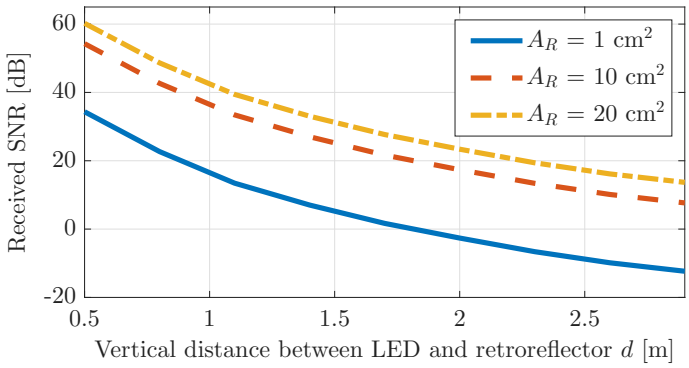


Fig. 11. Simulation of the received SNR versus vertical distance between LED-PD and retroreflector, for different retroreflector sizes (A_R) of Type XI and keeping all elements vertically aligned, i.e., $\alpha = 0°$ and $\beta = 0°$.

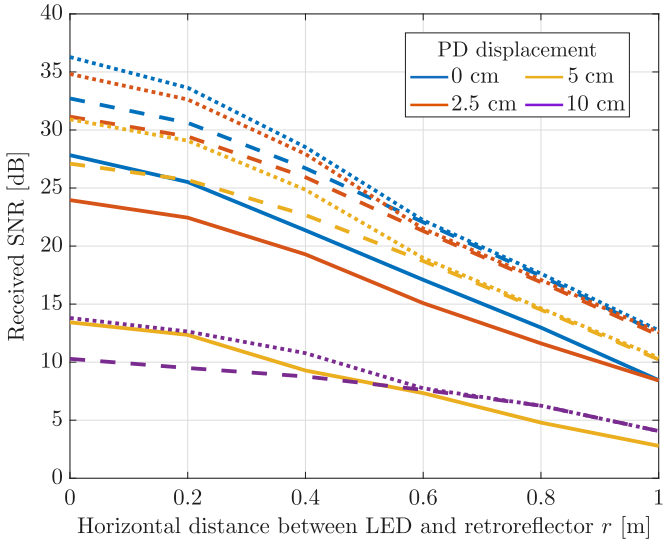


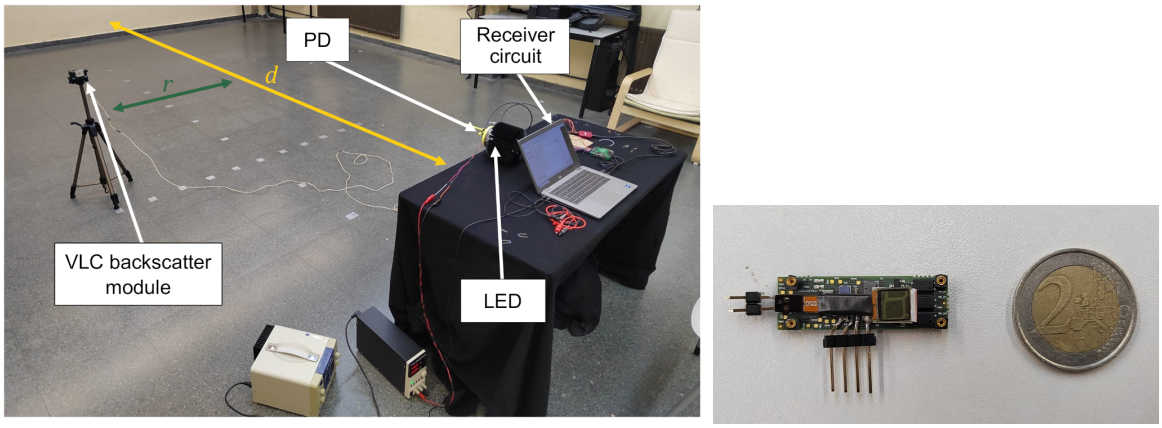
Fig. 12. Received SNR versus horizontal distance between LED/PD and retroreflector with $A_R = 10\,\text{cm}^2$, keeping a vertical distance of 1 m, and for different PD displacements with respect to the LED center. Solid line: retroreflector Type VII. Dashed line: retroreflector Type IX. Dotted line: retroreflector Type XI.

larger α and β as distance increases. Therefore, a more diffuse retroreflector provides larger SNR and better coverage for VLC backscatter.

Summary

The simulation results provide three practical insights directly informing the experimental evaluation:

(1) **SNR and active area:** practical amplifiers and envelope detection reduce SNR requirements, enabling reliable operation with retroreflector areas as small as 0.25 cm^2.



(a) Experimental setup.

(b) VLC backscatter module under test.

Fig. 13. Experimental setup and components used during the standalone evaluation.

(2) **Photodetector placement is dominant:** maximizing SNR requires placing the PD at the LED center to exploit the peak retroreflection efficiency, as we implement and validate experimentally in Section 7.
(3) **Diffuse retroreflectors outperform directive ones in realistic geometries:** This motivates the Type XI sheeting used in our MiniRetro prototype and confirmed experimentally in Sections 7 and 8.

7 Prototype Implementation and Experimental Characterization

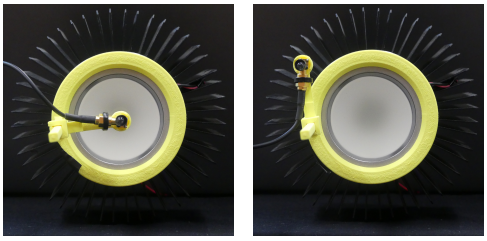
We implement the VLC backscatter setup depicted in Fig. 13a to experimentally evaluate the effect of the displacement of the PD presented in Section 6.

Transmitter. We use the LMH020-8000-35G9 from Cree [12] as light source, a widely used LED luminaire family for indoor illumination. We power the LED with a DC power supply at 43 V, providing a current of 0.8 A.

Backscatter module. The miniaturized VLC backscatter module is shown in Fig. 13b. It is mounted on a small Printed Circuit Board (PCB). We use the retroreflective sheeting 3M High Intensity Prismatic 3930 [2], classified as Type XI as in Fig. 10; the one exhibiting the best performance from the results in Section 6. The LC shutter is the 7×8 X-FOS(G2) of LC-Tec [23], with an active area of 5×5 mm^2, one of the smallest available on the market. We frame the shutter to the retroreflector at $\gamma = 60°$, as it maximizes the light power output, as shown in Fig. 9.

Receiver. On the receiver side, we use the PD SFH213 from Osram [35]. We shielded it with a layer of heat-shrink tubing to protect it from the direct light of the LED, and attach it to the LED frame with a 3D-printed holder. The PD is slightly separated from the LED to avoid heating the holder and the PD package. We test the PD at two positions: right over the center of the LED diffuser (Fig. 14a) and on its border (Fig. 14b). When used only for illumination, we would not want to block the LED light. But the impact of α on VLC backscatter performance requires careful PD positioning. The PD output connects via coaxial cable to a receiver board for signal conditioning.

The receiver circuit is shown in Fig. 15. The PD is connected to a *logarithmic transimpedance amplifier* (*log-TIA*). This configuration is well-known for optical applications, as human vision responds logarithmically to light, while natural illuminance varies exponentially across different environments and times of day. We AC-couple the PD to reject strong background DC light, including LED and sunlight itself. We observe no significant signal degradation at indoor sunlight levels (~800 lux) compared to measurements in the dark.



(a) PD on LED center. (b) PD on LED border.

Fig. 14. PD location with respect to the LED.

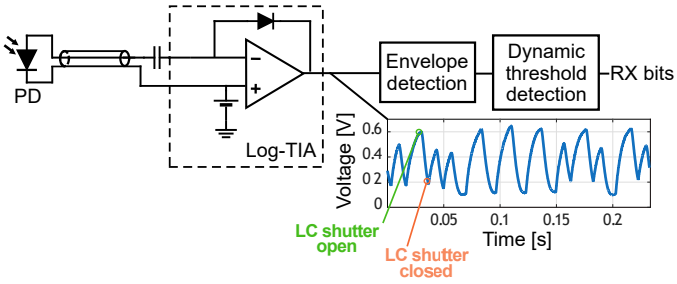


Fig. 15. VLC backscatter receiver circuit and analog received waveform.

By rejecting the DC component, we work at an operating point of the logarithmic curve providing very large gain while avoiding saturation. This is essential for detecting light reflected by the small area of the retroreflector. A DC source reverse-biases the PD and stabilizes the amplifier. We implement this stage using operational amplifiers OPA228 [42] and a diode 1N4148 [46] as a feedback element. Since our modulation uses only two symbols with different amplitudes, nonlinear distortion is avoided. The receiver circuit output is measured using an analog analyzer at 31.25 kSps.

Residual LED temperature drift produces low-frequency noise (a few Hz) at the receiver output even with thermal control. We apply *envelope detection* to remove it from the data signal. Then we compute a *dynamic decision threshold* based on the last 4 symbols, demodulate the signal and compute the bit error rate (BER).

Setup. We mount the VLC backscatter module on a tripod aligned in height with the LED. Multipath reflections are unlikely due to the directional nature of our link. By measuring in a wide indoor space, we emulate the scenario where the LED is used to illuminate the room.

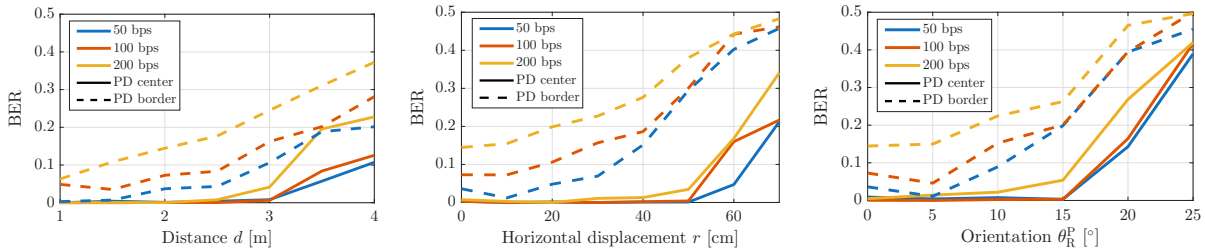
To characterize the VLC backscatter module, we modulate a standalone unit with a Manchester-encoded on-off keying (OOK) signal from a waveform generator. As recommended by the manufacturer, we use a bipolar signal without DC component to avoid damaging the shutter. We continuously transmit a 1 kbit sequence at 50, 100, and 200 bps, complying with the shutter's specified rise and fall times:

Distance. First, we modify the distance between the LED-PD transceiver with respect to the VLC backscatter module on the same optical axis (d in Fig. 13a). For the selected LED, we measure illuminance levels of 4075 lux, 1019 lux, and 453 lux at the VLC backscatter module for distances of 1 m, 2 m, and 3 m, respectively.

The results are plotted in Fig. 16a. We would expect better results with the PD on the border, since the LED light is less obstructed. However, the coefficient R_A and its dependence on α dominate. With the receiver centered, we reach a sufficiently low BER up to 3 m at 100 bps[4], worsening with the PD on the border. This shows the relevance of R_A in VLC backscatter with retroreflective sheeting, which greatly overcomes the effect of blocking the LED light. We must note the relatively small emitting area of this LED. This diffuser tends to be larger in real-life luminaries, so the relative blocked area of the emitting source would typically be smaller, and the performance gap between center and border PD locations much larger.

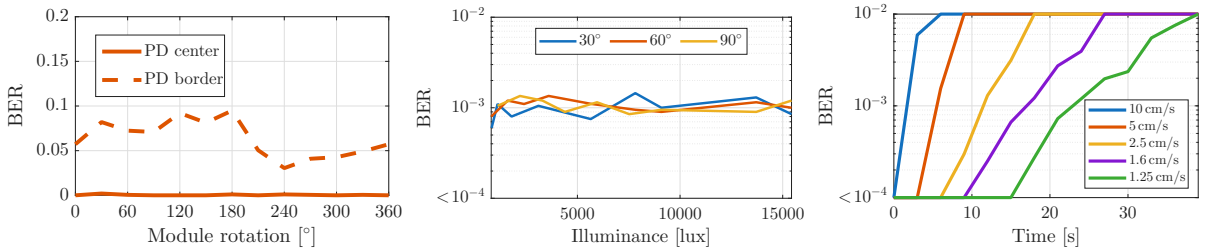
Horizontal displacement. This test evaluates system coverage. In a real deployment, each LED luminary can serve as an independent cell where the IoT device has sufficient mobility. This requires the link to remain reliable as the device moves away from the optical axis. We displace the VLC backscatter module perpendicularly to the optical axis at a fixed 2 m distance d. This is the range of a typical separation between an IoT device on a table or shelf and ceiling-mounted lights. Fig. 16b shows the link degrading with horizontal distance increasing from the origin. The PD in the center of the LED enables a cell with reliable communication with a radius of 50 cm,

[4]For the experimental figures, due to the low data rate, BER = 0 means BER $< 10^{-4}$.



(a) Distance (r = 0 cm and θ_R^P = 0°). (b) Displacement (d=2 m and θ_R^P = 0°). (c) Orientation (d=2 m and r = 0 cm).

Fig. 16. BER of MiniRetro for different data rates and PD placements.



(a) Rotation. (b) Background light. (c) Speed.

Fig. 17. Robustness of MiniRetro against rotation, background light, and movement (d=2 m, r = 0 cm and θ_R^P = 0°).

while the already deficient link with the PD on the border worsens further with displacement. This test shows the impact of the Lambertian emission, the retroreflection efficiency with β, and the field of view of the PD.

Orientation. Although most indoor IoT devices always have some surface pointing upwards, some are highly mobile and change orientation regularly. We test how robust MiniRetro is to this by modifying the orientation of the VLC backscatter module relative to the LED, which is equivalent to changing θ_R^P in Fig. 4, and monitor it using a magnetometer attached to the tripod. The results in Fig. 16c show a reliable link up to 15°. This may limit very mobile IoT environments such as wearables, although most stationary or robotic IoT devices lack the steering capability to tilt further than 15°.

Rotation. MiniRetro is robust against the rotation of the whole module, as shown in Fig. 17a, as it does not rely on polarized light on the receiver side. Therefore, we can rotate the module without impacting the performance. We perform this test at 100 bps and the default parameters used in Fig. 16. We observe negligible changes in BER with rotation, which means that we can safely rotate the IoT device around the optical axis. Given the symmetries on the experimental setup, this test, along with those on displacement and orientation, shows how robust MiniRetro is against misalignment.

Background light. We evaluate MiniRetro under varying background light to verify ambient illumination does not degrade communication. We fix the PD at the center of the LED and set the rate to 100 bps. We use an LED lamp to simulate a broad range of illuminance situations, from 500 to 15000 lux, by modifying its distance to MiniRetro. We also test incidence angles between 30°, 60°, and 90° to emulate light arriving from different directions. As seen in Fig. 17b, the BER remains in the order of 10^{-3} across the full range and is insensitive to incidence angle. This robustness follows from the AC-coupled, logarithmic receiver (Section 7), which rejects the DC background light under test. Further validation should determine whether MiniRetro can extend to outdoor conditions approaching direct sunlight.

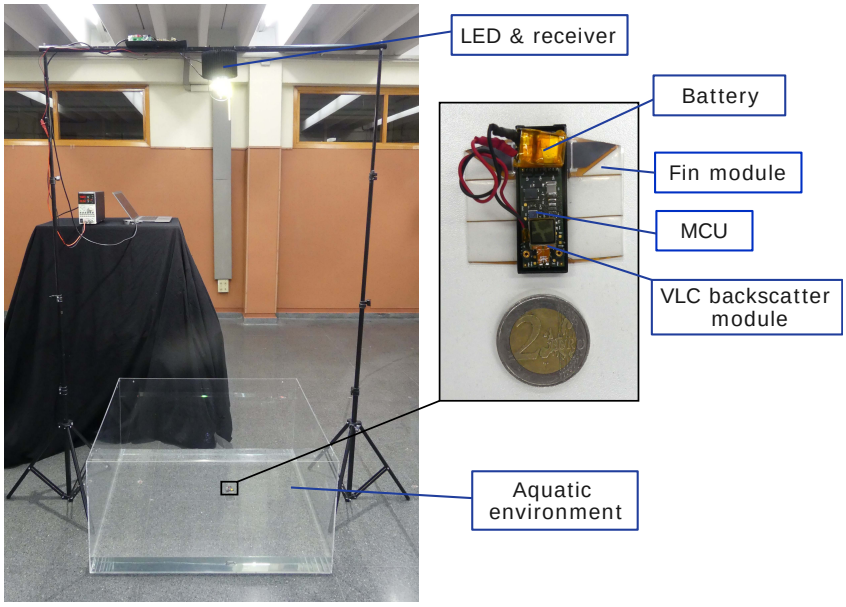


Fig. 18. Experimental setup for VLC backscatter communication for a swimming robot.

Mobility. The small form factor of MiniRetro enables deployment on moving platforms. We perform the same horizontal displacement as in Fig. 16b from $r = 0$ to 50 cm, at different speeds up to 10 cm/s, with ten repetitions per speed. Figure 17c shows the averaged BER against time for each speed. The increase in BER is approximately proportional to the speed in all cases. This reflects the time the module occupies positions receiving less optical power, rather than the actual impact of the speed. This implies that, within the tested range, motion itself does not degrade performance.

8 Application: Aquatic Robot

We propose MiniRetro as the uplink solution for a swimming robot performing sensing tasks in aquaponic facilities. These robots can self-redistribute to monitor a larger area than stationary systems, providing an in-depth mapping of the conditions of the aquaponics pond. Real-time mapping of the distribution of fertilizer, nutrients, by-products, and chemical compounds can lead to increased yield, ease automation, and reduce the environmental footprint of precision agriculture.

The lights used for stimulating crop growth or providing visibility to workers can be leveraged for VLC backscatter, usually placed at distances within the effective range of our link. The robots can move swiftly along aquaponics areas and through crops, navigating between VLC backscatter cells created by the lights. The high-pass filter from our receiver (Fig. 15) rejects low-frequency reflections, in the order of Hz, from the water surface or metallic structures. Sunlight exposure of the PD is minimized by the protective cone and its downward orientation, mitigating shot noise effects. Also, our link is resilient against robot inclination from wavy waters, as evaluated in Fig. 16c. Finally, the aquatic environment and the possibility of immersing the robot favour VLC over RF communications.

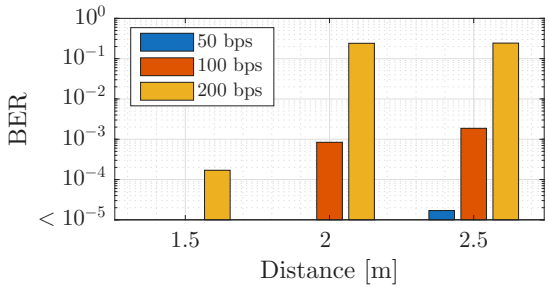


Fig. 19. BER for MiniRetro mounted on the swimming robot.

		50 bps	**100 bps**	**200 bps**
Standalone [μW]	Bipolar	76.23	110.88	110.88
	Unipolar	9.57	13.86	20.13
Robot [μW]	Bipolar	6016	6035	6031

Table 3. Power consumption of the standalone VLC backscatter module and the robot.

Implementation. We mount the VLC backscatter module on an 11×35 mm^2 PCB that controls a swimming fin system. The board includes an MKL02Z32 microcontroller unit (MCU), from NXP [34], an energy management unit, a thin-film chemical sensor area, and a high-voltage control system for the fins. The PCB is mounted on a case attached to a module of undulating fins, similarly to [19]. The modulating signal for the LC shutter is generated by the MCU and a dedicated XOR gate.

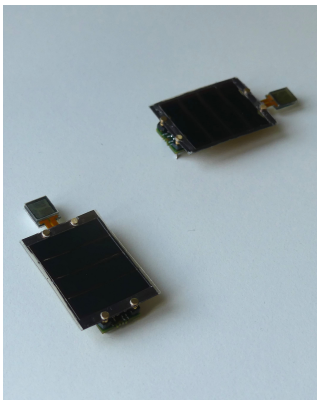
Note that, despite the PCB dimensions, the VLC backscatter components occupy less than 6 mm^2 of the PCB area. This leaves further space to miniaturize devices using this technology. We power the board with a Li-ion battery, since the energy harvester expects it to power the locomotion system. Nevertheless, given the low power draw of VLC backscatter, a more sustainable storage device, i.e., a supercapacitor, can power this communication alone. Fig. 18 shows the mounted robot and full experimental setup.

Evaluation. We evaluate MiniRetro mounted on the fin assembly, with the LED and receiver pointing vertically downward. We place a 100×85 cm^2 water tank below, emulating an aquaponics environment, with the robot floating on the surface. The robot transmits a fixed 64-bit packet (4-bit preamble) in a loop at different data rates. We decode and compute BER from the received bits, modifying the LED/receiver height to emulate different illumination conditions.

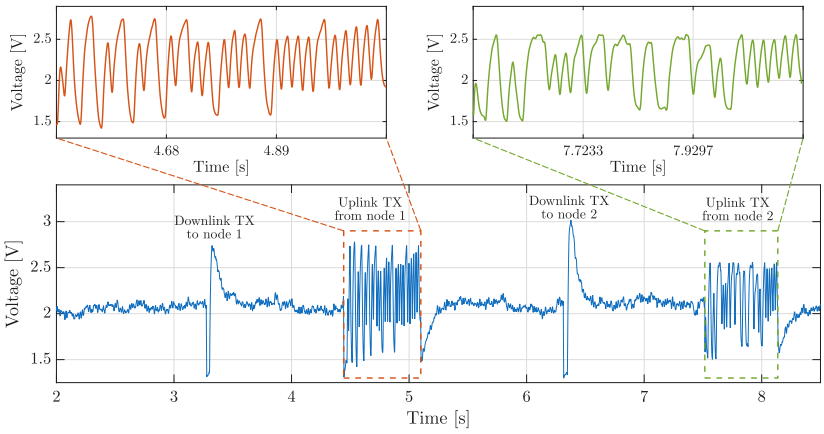
The results are shown in Fig. 19. We can appreciate how performance decreases as PD-robot distance increases, with limited impact from variations in horizontal displacement and orientation introduced by buoyancy over the water. Even at 2.5 m we can offer a reliable link at 50 bps, and at 100 bps with forward error correction (FEC). This type of small monitoring robot requires very modest data rates, mainly to send identifiable sensor readings or localization coordinates to a control station. These results are consistent across the water tank, meaning a VLC backscatter cell covers this entire area.

Power consumption. In order to assess the sustainability of our system, we measure the power consumption both standalone and when mounted on the robot. For the standalone version, we compute the consumed power by measuring the current and voltage through the LC shutter while modulating.

Table 3 shows the results. Modulating an LC shutter requires carefully considering the signal to use. Applying OOK voltage directly (0 V for '0', nonzero for '1', the *unipolar* method) involves applying a DC component,



(a) Robot PCB with solar cells for optical downlink.



(b) Multiple node management through downlink VLC channel.

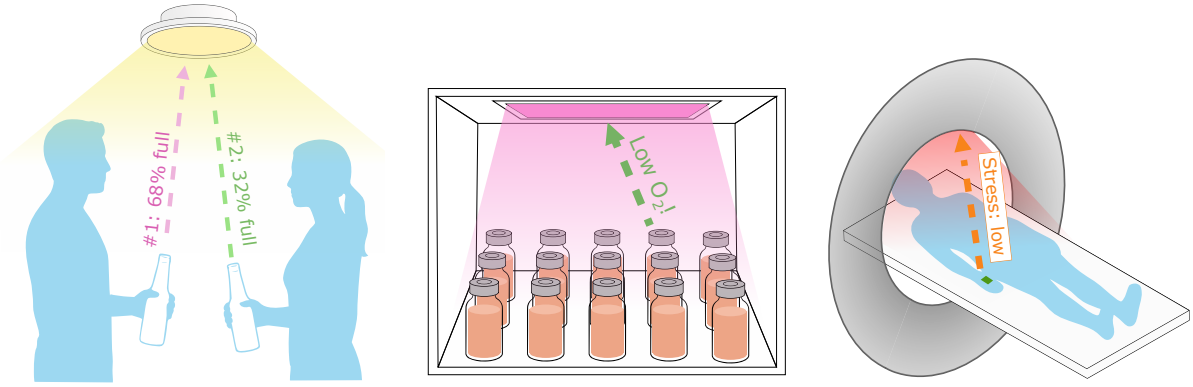
Fig. 20. Multiple node experiment.

which risks shutter damage from charge accumulation and persistent alignment of LC molecules, which degrades performance over time. The *bipolar* method proves safer as it instead encodes symbol '1' as a voltage signal at a frequency the shutter cannot follow (e.g., 10 kHz). This produces a similar backscattered signal strength without damaging the shutter. The drawback is a higher power consumption, as the LC molecules try to follow the AC signal. Choosing between them trades off device lifetime against power consumption.

The standalone module results show a significant difference between methods, meaning they involve an important design criterion. We can appreciate how power consumption increases with data rate as voltage transitions demand more current from the shutter. Interestingly, bipolar signaling at 100 and 200 bps draws the same power, likely because the shutter cannot follow the 200 bps bipolar signal, which may also explain its limited results. We also show the power consumption of the robot, which shows no difference across data rates, since the VLC backscatter module draws negligible power relative to the rest of the robot. The power consumed by sensing and communication is orders of magnitude below that of driving the fin system. Energy savings are therefore largely determined by the duty cycle of each task: as an example, in the aquaponics farm environment, sensing is expected to occur much more often than locomotion.

Multi-node setup. In the preceding experiments, each robot operated as a passive, uplink-only backscatter node. In a realistic deployment, however, several mobile robots share the illumination area of a single LED, and the base station must be able to *address* an individual robot—instructing a specific node when to report—in order to collect data from many of them without collisions. This requirement is what motivates a downlink channel, complementing the visible-light backscatter uplink, which on its own cannot select among mobile nodes.

We orchestrate multiple access via time division. Note that every LED bulb illuminates a small area that can contain very few IoT devices. This makes time-division orchestration much easier. To this end, we introduce a downlink channel between a base station and the robots, which serves as the addressing and scheduling mechanism that lets the base station select which mobile node transmits and when. The robot PCB exposes a connection for a solar cell that serves the dual purpose of energy harvesting and receiving a conventional VLC signal, following the design described in [33]. For the base station, which orchestrates the deployed robots, we modulate the LED that provides the carrier signal for VLC backscatter, thereby generating a downlink signal received by the solar cell on each robot. This downlink VLC channel with a solar cell as receiver preserves the low-power and RF-free requirements of the application [40].



(a) Consumer monitoring. (b) Vial monitoring. (c) Medical RF-free.

Fig. 21. Other potential applications of MiniRetro.

For this receiver, we attach thin-film perovskite solar cells, similar to those described in [18], to the robot PCBs, as shown in Fig 20a. On a weight-constrained swimming robot, the decisive figure of merit is *specific power* (power per unit weight) rather than absolute conversion efficiency, and these flexible cells combine high specific power with improved operational stability in humid conditions. We relocated the VLC backscatter module outside the main PCB layout to prevent the solar cell from occluding it. We replicate the setup from Fig. 18 with both nodes, fixing the distance between the LED and the plane of the PCBs at 2 m, and modulating the LED to transmit an OOK signal at 1 kHz. This configuration establishes a bidirectional link that now supports multiple access. Each robot is programmed to transmit a fixed 64-bit uplink packet at 100 bps upon receiving a specific 32-bit codeword from the LED. This emulates actual readings from sensors that can be integrated into the robot.

Figure 20b shows the output of the VLC backscatter receiver for this test. This downlink transmission is captured by the VLC backscatter receiver and interferes with the uplink channel, meaning that downlink and uplink cannot operate concurrently during orchestration and time-division multiplexing is required. Node 1 transmits its fixed packet one second after receiving the downlink instruction, emulating the time required to perform and process sensor readings. The procedure is then repeated for node 2. We can see how each robot correctly identifies the codeword addressed to it and the nodes do not respond concurrently, with both uplink responses clearly separable. The signal from node 1 is also slightly stronger than that of node 2, due to its closer distance to the LED at the time. This test demonstrates that a practical MAC-layer protocol is feasible even for autonomous designs of this form factor.

9 Other applications

Besides the aquaponic use case, several scenarios can benefit from MiniRetro. The common pattern is per-item monitoring at large scale, where fixed sensing infrastructure is impractical and RF is undesirable or physically impossible; sensing, telemetry, presence detection, and identification are well matched to the data rate provided. Below, we show three new applications, conceptualized in Fig. 21, enabled by the main contributions of our work: absence of RF hardware, low power consumption, directional links, and system miniaturization.

- **Consumer tracking**: Monitoring human interaction with domestic elements is useful in many environments, especially for low-cost or disposable items. For example, tracking the available liquid across a large number of beverages in a bar, restaurant, or event can help the management and staff to provide

better service. Sensing this wirelessly, e.g., by computer vision, can raise privacy concerns and requires dense video deployments. However, unobtrusive low-power sensors placed in glasses or bottles can extract this information [3, 28]. VLC backscatter can serve as an uplink solution for such sensors, with a module integrated on the superior border of the glass or bottle. A regular soda bottle offers an area of~2.7 cm^2 on the top ring-shaped border, roughly an order of magnitude larger than MiniRetro's footprint.

- **Biomedical asset monitoring**: In the biological and pharmaceutical industries, large numbers of vials must be kept under tightly controlled conditions to preserve product stability or support ongoing bioprocesses. Since identical vials under shared conditions can yield different outcomes, individual monitoring is desirable. However, deploying dedicated technicians or robotic handlers for per-vial inspection is costly and hard to scale. Vials can instead be monitored inside storage cabinets and report properties live. Recent research on nanowire sensors offers a low-power, cost-effective alternative for monitoring chemicals [37, 43], which can be embedded in contact with the sample or the headspace. A cabinet illuminating an array of vials from above, for visibility, heating, or process needs, also provides a carrier for VLC backscatter: sensed parameters can be reported by placing the transmitter on the vial's lid or rim. A typical lid offers an area close to ~1 cm^2 to accommodate a VLC backscatter transmitter. This reduces the complexity of arranging sensing equipment in the cabinet, which is harder to replace than a malfunctioning vial, and avoids the use of RF for a very dense distribution of nodes inside a metallic enclosure.
- **Medical applications**: In magnetic resonance imaging (MRI), patients must remain under continuous physiological monitoring to ensure safety and correlate clinical signals with the acquired images [14]. Several sensors are already prepared to withstand the strong magnetic field inside an MRI machine [31]. But conventional RF-based wireless devices cannot operate inside the MRI bore, while wired alternatives restrict patient movement and limit monitoring points. A VLC backscatter link can instead report this information to a receiver integrated inside the machine, with a small optical aperture receiving from multiple sensors. Transmitters can be coupled with sensors in adhesive skin patches, in contact with the skin or integrated sensing electrodes, each presenting roughly 1 cm^2 to host the module.

10 System limitations

While miniaturization enables new applications, several limitations remain that motivate future work. Regarding data rate, we find two fundamental ways to increase it. First, exploiting alternative shutter modulation, as done by previous works leveraging the polarization and relaxation times of LC [38, 49, 51]. Second, a fundamentally faster way to modulate light and/or employ multiple elements simultaneously: faster LC alternatives such as pi-cells or ferroelectric LCs decrease response time to the microsecond regime [26, 50], typically at the cost of higher drive voltages. The most aligned competitors are digital micro-mirrors (DMD), which deliver a much larger data rate [52].

The rest of these parameters shown in this study fall within the limits for several applications. Indoor spaces, including walls, shelves, racks, desks, etc., can fit several miniaturized tags, and the mobility of objects carrying such tags complies with the range and orientation limits presented in our study, considering regular indoor lighting as the carrier. But the range can also be extended for the same tag size with a portable directive light source interrogating the tag [24]. The directionality of the link provides spatial confinement with two advantages: intrinsic physical privacy in identification tasks, and minimal interference with simpler coordination, translating into less complex protocols and longer sleep duty cycles for low-power devices. Finally, operating outside the RF spectrum makes these tags deployable in RF-sensitive or restricted environments.

Regarding cost, LC shutters do not usually come in miniaturized packages, but the manufacturing process is suitable for producing very small shutters at low cost [16]. At mm-scale, raw material costs can be decreased below a dollar, with the retroreflector required below a cent per module [1], making them easily disposable. Processing

units sufficient to read a sensor and drive a VLC backscatter transmitter are also low-cost: an ARM-Cortex-M0+ chip, as used in Section 8, can be found for a few cents. With an inexpensive sensor too, this yields a low-cost, even disposable, monitoring alternative. For self-sustainability, a small energy buffer (capacitor) and source (solar cell) can be used.

11 Conclusion

We presented MiniRetro, a miniaturized VLC backscatter system that combines liquid crystal shutters with retroreflective sheetings to enable sustainable and compact IoT connectivity. Through analytical modeling, simulations, and experimental validation, we characterized the impact of geometry, polarization, and transmittance on link performance. Our prototype achieves reliable meter-scale communication with an active area of only 0.25 cm^2, making it the first VLC backscatter design operating with a sub-cm^2 active area. Under a FOM metric accounting for system size, range, and power efficiency, it scores 6× higher than prior work. These results position MiniRetro as a practical and scalable approach for low-power miniaturized IoT communication leveraging lighting infrastructure.

Acknowledgments

This work has been partially funded by the European Union Horizon 2020 Research and Innovation Action SOMIRO, under Grant Agreement No. 101016411; by project TEC-2024/COM-460 (TUCAN6-CM), funded by CM (ORDEN 5696/2024); by Ramón y Cajal grant RYC2023-042518-I, funded by MCIU/AEI/10.13039/501100011033 and FSE+; and by project PID2024-156038OA-I00 (HOLIFI6G) by MICIU /AEI /10.13039/501100011033 / FEDER, UE. The authors would like to thank the researchers from the Soft Transducers Lab of EPFL for providing fin modules to test our system.

A Appendix

Jones Matrices for Corner-Cube Retroreflector. A corner-cube retroreflector has six reflection possibilities and therefore six Jones matrices [27], shown below:

$$
\begin{aligned}
J_{123} &= \begin{bmatrix} -0.0266 + 0.9586i & 0.2282 + 0.1685i \\ 0.2282 + 0.1685i & -0.9083 + 0.3075i \end{bmatrix} \\
J_{231} &= \begin{bmatrix} 0.6746 + 0.0090i & -0.1766 + 0.7167i \\ 0.6330 - 0.3797i & -0.2071 - 0.6421i \end{bmatrix} \\
J_{312} &= \begin{bmatrix} 0.6746 + 0.0090i & 0.6330 - 0.3797i \\ -0.1766 + 0.7167i & -0.2071 - 0.6421i \end{bmatrix} \\
J_{321} &= \begin{bmatrix} -0.0266 + 0.9586i & -0.2282 - 0.1685i \\ -0.2282 - 0.1685i & -0.9083 + 0.3075i \end{bmatrix} \\
J_{132} &= \begin{bmatrix} 0.6746 + 0.0090i & -0.6330 + 0.3797i \\ 0.1766 - 0.7167i & -0.2071 - 0.6421i \end{bmatrix} \\
J_{213} &= \begin{bmatrix} 0.6746 + 0.0090i & 0.1766 - 0.7167i \\ -0.6330 + 0.3797i & -0.2071 - 0.6421i \end{bmatrix}.
\end{aligned}
\tag{12}
$$

From the Jones matrices, we can compute the output polarization vector for a region j as

$$
\mathbf{E}_j = J_{abc}\,\mathbf{a}, \tag{13}
$$

where

$$\mathbf{a} = \begin{pmatrix} E_H \\ E_V \end{pmatrix} \tag{14}$$

is the input light's polarization vector, with E_H and E_V the normalized horizontal and vertical field amplitudes.

Since the six regions in a single retroreflector have the same size, we assume each output polarization is equally probable. The output intensity after unpolarized light passes twice through the LC shutter polarizing in direction $\mathbf{a}$ can be computed as

$$I_{LC,2}(\mathbf{a}) = \frac{1}{6} \sum_{j=1}^{6} |\mathbf{E}_j \cdot \mathbf{a}|^2. \tag{15}$$

As both vectors $\mathbf{E}_j$ and $\mathbf{a}$ are normalized, the intensity $I_{LC,2}(\mathbf{a})$ eventually becomes $\rho_{pol,2}$, indicating how much light is lost from the retroreflector to the other side of the shutter. The dot product $|\mathbf{E}_j \cdot \mathbf{a}|$ means that only that fraction of light aligned in the polarization direction $\mathbf{a}$ will exit the LC shutter.[5]

From (15), we can derive the optimal polarization vector $\mathbf{a}$ to use in our VLC backscatter module. In practice, this vector is determined by the angle γ in Fig. 7. This is the relative angle between the LC shutter and the retroreflective sheeting in the x-y plane, representing the rotation of the sheeting around the z axis perpendicular to both.

References

[1] 3M. 2016. 3M Diamond Grade 4090 Series. Retrieved February 1, 2026 from https://www.3m.com/3M/en_US/p/d/b00011967

[2] 3M. 2016. Diamond Grade™ DG³ Prismatic Digital Sheeting 4090DS. Retrieved February 1, 2026 from https://multimedia.3m.com/mws/media/1184590O/3m-diamond-grade-dg3-prismatic-digital-sheeting-4090ds-white.pdf

[3] Chamath Amarasinghe and Nimesha Ranasinghe. 2022. SipBit: A Sensing Platform to Recognize Beverage Type, Volume, and Sugar Content Using Electrical Impedance Spectroscopy and Deep Learning. In *Extended Abstracts of the 2022 CHI Conference on Human Factors in Computing Systems* (New Orleans, LA, USA) *(CHI EA '22)*. Association for Computing Machinery, New York, NY, USA, Article 371, 8 pages. doi:10.1145/3491101.3519713

[4] ASTM International. 2013. *Standard Test Method for Coefficient of Retroreflection of Retroreflective Sheeting Utilizing the Coplanar Geometry*. Standard ASTM E810-03. American Society for Testing and Materials, West Conshohocken, US. doi:10.1520/E0810-03R13

[5] ASTM International. 2019. *Standard Specification for Retroreflective Sheeting for Traffic Control*. Standard ASTM D4956-19. American Society for Testing and Materials, West Conshohocken, US. doi:10.1520/D4956-19

[6] Rens Bloom, Marco Zúñiga Zamalloa, and Chaitra Pai. 2019. LuxLink: creating a wireless link from ambient light. In *Proceedings of the 17th Conference on Embedded Networked Sensor Systems* (New York, New York) *(SenSys '19)*. ACM, New York, NY, USA, 166–178. doi:10.1145/3356250.3360021

[7] Charles J. Carver, Hadleigh Schwartz, Qijia Shao, Nicholas Shade, Joseph Lazzaro, Xiaoxin Wang, Jifeng Liu, Eric Fossum, and Xia Zhou. 2024. Catch Me If You Can: Laser Tethering with Highly Mobile Targets. In *Proceedings of the 21st USENIX Symposium on Networked Systems Design and Implementation (NSDI 24)*. USENIX Association, Santa Clara, CA, 1847–1865. https://www.usenix.org/conference/nsdi24/presentation/carver

[8] Charles J. Carver, Qijia Shao, Samuel Lensgraf, Amy Sniffen, Maxine Perroni-Scharf, Hunter Gallant, Alberto Quattrini Li, and Xia Zhou. 2022. Sunflower: locating underwater robots from the air. In *Proceedings of the 20th Annual International Conference on Mobile Systems, Applications and Services* (Portland, Oregon) *(MobiSys '22)*. ACM, New York, NY, USA, 14–27. doi:10.1145/3498361.3539773

[9] Charles J. Carver, Zhao Tian, Hongyong Zhang, Kofi M. Odame, Alberto Quattrini Li, and Xia Zhou. 2020. AmphiLight: Direct Air-Water Communication with Laser Light. In *Proceedings of the 17th USENIX Symposium on Networked Systems Design and Implementation (NSDI 20)*. USENIX Association, Santa Clara, CA, 373–388. https://www.usenix.org/conference/nsdi20/presentation/carver

[10] Yoon Chae, Zhenzhe Lin, Kang Min Bae, Song Min Kim, and Parth Pathak. 2024. mmComb: high-speed mmWave commodity WiFi backscatter. In *Proceedings of the 21st USENIX Symposium on Networked Systems Design and Implementation* (Santa Clara, CA, USA) *(NSDI'24)*. USENIX Association, USA, Article 94, 17 pages. https://www.usenix.org/conference/nsdi24/presentation/chae

[11] Ricardo Correia and Nuno Borges Carvalho. 2017. Ultrafast Backscatter Modulator With Low-Power Consumption and Wireless Power Transmission Capabilities. *IEEE Microwave and Wireless Components Letters* 27, 12 (2017), 1152–1154. doi:10.1109/LMWC.2017.2760739

[12] Cree LED. 2022. LMH2 LED Modules Family. Retrieved February 1, 2026 from https://downloads.cree-led.com/files/ds/m/LMH2.pdf

[5] This equation is the formulation in optical algebra for Malus' law: $I = I_0 \cos^2(\phi)$.

[13] Lucan De Groot, Talia Xu, and Marco Zúñiga Zamalloa. 2023. DroneVLC: Exploiting Drones and VLC to Gather Data from Batteryless Sensors. In *Proceedings of the IEEE International Conference on Pervasive Computing and Communications (PerCom)*. IEEE, Piscataway, NJ, USA, 242–251. doi:10.1109/PERCOM56429.2023.10099247

[14] P. Fraga Rivas, J. de Miguel Criado, L. García del Salto Lorente, L. Gutiérrez Velasco, and P. Quintana Valcarcel. 2023. Patient safety in magnetic resonance imaging. *Radiología (English Edition)* 65, 5 (2023), 447–457. doi:10.1016/j.rxeng.2023.01.009

[15] Seyed Keyarash Ghiasi, Marco A. Zúñiga Zamalloa, and Koen Langendoen. 2021. A Principled Design for Passive Light Communication. In *Proceedings of the 27th Annual International Conference on Mobile Computing and Networking* (New Orleans, Louisiana) *(MobiCom '21)*. ACM, New York, NY, USA, 121–133. doi:10.1145/3447993.3448629

[16] Yan Gong, Bo Li, Cheng-You Yao, Weiyang Yang, Qi Hua Fan, Zhen Qiu, and Wen Li. 2022. Tunable, Low–Cost, Multi–Channel, Broadband Liquid Crystal Shutter for Fluorescence Imaging in Widefield Microscopy. *Micromachines* 13, 8 (2022), 1310. doi:10.3390/mi13081310

[17] Bowen Gu, Dong Li, Haiyang Ding, Gongpu Wang, and Chintha Tellambura. 2025. Breaking the interference and fading gridlock in backscatter communications: State-of-the-art, design challenges, and future directions. *IEEE Communications Surveys & Tutorials* 27, 2 (2025), 870–911. doi:10.1109/COMST.2024.3436082

[18] Bekele Hailegnaw, Stepan Demchyshyn, Christoph Putz, Lukas E. Lehner, Felix Mayr, David Schiller, Roland Pruckner, Munise Cobet, Dorian Ziss, Tobias Maria Krieger, Armando Rastelli, Niyazi Serdar Sariciftci, Markus Clark Scharber, and Martin Kaltenbrunner. 2024. Flexible quasi-2D perovskite solar cells with high specific power and improved stability for energy-autonomous drones. *Nature Energy* 9, 6 (01 Jun 2024), 677–690. doi:10.1038/s41560-024-01500-2

[19] Florian Hartmann, Mrudhula Baskaran, Gaetan Raynaud, Mehdi Benbedda, Karen Mulleners, and Herbert Shea. 2025. Highly agile flat swimming robot. *Science Robotics* 10, 99 (2025), eadr0721. doi:10.1126/scirobotics.adr0721

[20] Gaojian Huang, Yuxin Lei, Shuanggen Jin, Yuan Ding, Liang Chen, Xingwang Li, and Arumugam Nallanathan. 2025. Backscatter Directional Modulation Communication Using Time Modulated Van-Atta Arrays. *IEEE Transactions on Vehicular Technology* 74, 11 (2025), 17503–17513. doi:10.1109/TVT.2025.3578782

[21] Yong-Liang Huang and Chi-Kuang Sun. 2000. Nonlinear saturation behaviors of high-speed p-i-n photodetectors. *Journal of Lightwave Technology* 18, 2 (2000), 203–212. doi:10.1109/50.822794

[22] Tao Jiang, Yu Zhang, Wenyuan Ma, Miaoran Peng, Yuxiang Peng, Mingjie Feng, and Guanghua Liu. 2023. Backscatter Communication Meets Practical Battery-Free Internet of Things: A Survey and Outlook. *IEEE Communications Surveys & Tutorials* 25, 3 (2023), 2021–2051. doi:10.1109/COMST.2023.3278239

[23] LC-Tec Displays AB. 2016. X-FOS(G2)/X-FOS(G2)-AR Product Specification. Retrieved February 1, 2026 from https://www.lc-tec.se/wp-content/uploads/2019/05/X-FOSG2_X-FOSG2-AR-specification-1602.pdf

[24] Walter D. Leon-Salas and Xiaozhe Fan. 2018. Exploiting Luminescence Emissions of Solar Cells for Optical Frequency Identification (OFID). In *2018 IEEE International Symposium on Circuits and Systems (ISCAS)*. IEEE, Florence, Italy, 1–5. doi:10.1109/ISCAS.2018.8351139

[25] Jiangtao Li, Angli Liu, Guobin Shen, Liqun Li, Chao Sun, and Feng Zhao. 2015. Retro-VLC: Enabling Battery-free Duplex Visible Light Communication for Mobile and IoT Applications. In *Proceedings of the 16th International Workshop on Mobile Computing Systems and Applications* (Santa Fe, New Mexico, USA) *(HotMobile '15)*. ACM, New York, NY, USA, 21–26. doi:10.1145/2699343.2699354

[26] Yannanqi Li, Zhiyong Yang, Ran Chen, Lingchao Mo, Juanli Li, Minggang Hu, and Shin-Tson Wu. 2020. Submillisecond-Response Polymer Network Liquid Crystal Phase Modulators. *Polymers* 12, 12 (2020), 2862. doi:10.3390/polym12122862

[27] Jian Liu and Rafig Azzam. 1997. Polarization properties of corner-cube retroreflectors: Theory and experiment. *Applied Optics* 36 (04 1997), 1553–9. doi:10.1364/AO.36.001553

[28] Mengxi Liu, Sizhen Bian, Bo Zhou, Agnes Gruenerbl, and Paul Lukowicz. 2022. Smart Cup: An impedance sensing based fluid intake monitoring system for beverages classification and freshness detection. In *Adjunct Proceedings of the 2022 ACM International Joint Conference on Pervasive and Ubiquitous Computing and the 2022 ACM International Symposium on Wearable Computers* (Cambridge, United Kingdom) *(UbiComp/ISWC '22 Adjunct)*. Association for Computing Machinery, New York, NY, USA, 78–80. doi:10.1145/3544793.3560326

[29] John Lloyd. 2008. A brief history of retroreflective sign face sheet materials. Retrieved February 1, 2026 from https://www.rema.org.uk/pub/pdf/history-retroreflective-materials.pdf

[30] Haofan Lu, Mohammad Mazaheri, Reza Rezvani, and Omid Abari. 2023. A Millimeter Wave Backscatter Network for Two-Way Communication and Localization. In *Proceedings of the ACM SIGCOMM 2023 Conference* (New York, NY, USA) *(ACM SIGCOMM '23)*. Association for Computing Machinery, New York, NY, USA, 49–61. doi:10.1145/3603269.3604873

[31] Bruno Madore, Aaron T. Hess, Adam M. J. van Niekerk, Daniel C. Hoinkiss, Patrick Hucker, Maxim Zaitsev, Onur Afacan, and Matthias Günther. 2022. External Hardware and Sensors, for Improved MRI. *Journal of Magnetic Resonance Imaging* 57, 3 (Nov. 2022), 690–705. doi:10.1002/jmri.28472

[32] Mohammad Hossein Mazaheri, Alex Chen, and Omid Abari. 2021. mmTag: a millimeter wave backscatter network. In *Proceedings of the 2021 ACM SIGCOMM 2021 Conference* (Virtual Event, USA) *(SIGCOMM '21)*. Association for Computing Machinery, New York, NY, USA, 463–474. doi:10.1145/3452296.3472917

[33] Muhammad Sarmad Mir, Borja Genoves Guzman, Ambuj Varshney, and Domenico Giustiniano. 2021. PassiveLiFi: Rethinking LiFi for Low-Power and Long Range RF Backscatter. In *Proceedings of the 27th Annual International Conference on Mobile Computing and*

Networking (New Orleans, Louisiana) *(MobiCom '21)*. ACM, New York, NY, USA, 697–709. doi:10.1145/3447993.3483262

[34] NXP Semiconductors. 2017. Kinetis KL02 32 KB Flash. Retrieved February 1, 2026 from https://www.nxp.com/docs/en/data-sheet/KL02P32M48SF0.pdf

[35] Osram. 2022. *SFH 213 Datasheet*. Retrieved February 1, 2026 from https://look.ams-osram.com/m/236756eb2a4c9193/original/SFH-213.pdf

[36] Umair Mujtaba Qureshi, Faisal Karim Shaikh, Zuneera Aziz, Syed M. Zafi S. Shah, Adil A. Sheikh, Emad Felemban, and Saad Bin Qaisar. 2016. RF Path and Absorption Loss Estimation for Underwater Wireless Sensor Networks in Different Water Environments. *Sensors* 16, 6 (2016), 890. doi:10.3390/s16060890

[37] Srinivasan Raman, Ravi Sankar A, and Sindhuja M. 2023. Advances in silicon nanowire applications in energy generation, storage, sensing, and electronics: a review. *Nanotechnology* 34, 18 (Feb. 2023), 182001. doi:10.1088/1361-6528/acb320

[38] Sihua Shao, Abdallah Khreishah, and Hany Elgala. 2017. Pixelated VLC-Backscattering for Self-Charging Indoor IoT Devices. *IEEE Photonics Technology Letters* 29, 2 (2017), 177–180. doi:10.1109/LPT.2016.2631946

[39] Sihua Shao, Adrian Salustri, Alexander Heusser, Hassan Khaniani, Mostafa Hassanalian, and Pedram Roghanchi. 2024. Downlink-Uplink Symmetry in Mobile Battery-Free Retro-Reflective VLC: Enabling Sensing-Assisted Communications. In *Proceedings of the IEEE International Conference on Communications Workshops (ICC Workshops)*. IEEE, Piscataway, NJ, USA, 1061–1066. doi:10.1109/ICCWorkshops59551.2024.10615381

[40] Javier Talavante, Borja Genoves Guzman, and Domenico Giustiniano. 2025. Solar Cell Operating Point for Joint LiFi Communication and Harvesting in Battery-Free Devices. *IEEE Transactions on Communications* 73, 12 (Aug. 2025), 14725–14738. doi:10.1109/TCOMM.2025.3599896

[41] Javier Talavante, Borja Genoves Guzman, and Domenico Giustiniano. 2023. Rethinking LiFi for Carbon Neutral Sunlight-based Communication. In *Proceedings of the 21st Mediterranean Communication and Computer Networking Conference (MedComNet)*. IEEE, Piscataway, NJ, USA, 53–60. doi:10.1109/MedComNet58619.2023.10168863

[42] Texas Instruments. 2023. OPA228 Precision, Low Noise, Low Offset Operational Amplifier. Retrieved February 1, 2026 from https://www.ti.com/lit/ds/symlink/opa228.pdf

[43] To Thi Nguyet, Lai Van Duy, Nguyen Cao Nam, Do Quang Dat, Hugo Nguyen, Chu Manh Hung, Nguyen Van Duy, and Nguyen Duc Hoa. 2025. Transition from p-type to n-type semiconductor in V2O5 nanowire-based gas sensors: Synthesis and understanding of the sensing mechanism. *Sensors and Actuators B: Chemical* 424 (2025), 136841. doi:10.1016/j.snb.2024.136841

[44] Thorlabs. 2020. TIR Retroreflector Prisms. Retrieved February 1, 2026 from https://www.thorlabs.com/newgrouppage9.cfm?objectgroup_id=145

[45] Muhammad Habib Ullah, Giacinto Gelli, and Francesco Verde. 2023. Visible light backscattering with applications to the Internet of Things: State-of-the-art, challenges, and opportunities. *Internet of Things* 22 (2023), 100768. doi:10.1016/j.iot.2023.100768

[46] Vishay. 2024. 1N4148 Small Signal Fast Switching Diodes. Retrieved February 1, 2026 from https://www.vishay.com/docs/81857/1n4148.pdf

[47] Purui Wang, Lilei Feng, Guojun Chen, Chenren Xu, Yue Wu, Kenuo Xu, Guobin Shen, Kuntai Du, Gang Huang, and Xuanzhe Liu. 2020. Renovating road signs for infrastructure-to-vehicle networking: a visible light backscatter communication and networking approach. In *Proceedings of the 26th Annual International Conference on Mobile Computing and Networking* (London, United Kingdom) *(MobiCom '20)*. ACM, New York, NY, USA, Article 6, 13 pages. doi:10.1145/3372224.3380883

[48] Yue Wu, Purui Wang, and Chenren Xu. 2019. Demo: Improving Visible Light Backscatter Communication with Delayed Superimposition Modulation. In *Proceedings of the 25th Annual International Conference on Mobile Computing and Networking* (Los Cabos, Mexico) *(MobiCom '19)*. ACM, New York, NY, USA, Article 71, 3 pages. doi:10.1145/3300061.3343364

[49] Yue Wu, Purui Wang, Kenuo Xu, Lilei Feng, and Chenren Xu. 2020. Turboboosting Visible Light Backscatter Communication. In *Proceedings of the Annual Conference of the ACM Special Interest Group on Data Communication on the Applications, Technologies, Architectures, and Protocols for Computer Communication* (Virtual Event, USA) *(SIGCOMM '20)*. ACM, New York, NY, USA, 186–197. doi:10.1145/3387514.3406229

[50] Peter J. M. Wyatt, James Bailey, Mamatha Nagaraj, and J. Cliff Jones. 2021. A self-healing ferroelectric liquid crystal electro-optic shutter based on vertical surface-relief grating alignment. *Nature Communications* 12 (2021), 4717. doi:10.1038/s41467-021-24953-5

[51] Kenuo Xu, Chen Gong, Bo Liang, Yue Wu, Boya Di, Lingyang Song, and Chenren Xu. 2022. Low-latency visible light backscatter networking with RetroMUMIMO. In *Proceedings of the 20th ACM Conference on Embedded Networked Sensor Systems*. ACM, New York, NY, USA, 448–461. doi:10.1145/3560905.3568507

[52] Talia Xu, Miguel Chávez Tapia, and Marco Zúñiga. 2022. Exploiting Digital Micro-Mirror Devices for Ambient Light Communication. In *19th USENIX Symposium on Networked Systems Design and Implementation (NSDI 22)*. USENIX Association, Renton, WA, 387–400. https://www.usenix.org/conference/nsdi22/presentation/xu-talia

[53] Xieyang Xu, Yang Shen, Junrui Yang, Chenren Xu, Guobin Shen, Guojun Chen, and Yunzhe Ni. 2017. PassiveVLC: Enabling Practical Visible Light Backscatter Communication for Battery-Free IoT Applications. In *Proceedings of the 23rd Annual International Conference on Mobile Computing and Networking* (Snowbird, Utah, USA) *(MobiCom '17)*. ACM, New York, NY, USA, 180–192. doi:10.1145/3117811.3117843

[54] Jihui Yuan, Zhichao Jiao, Xiangfei Kong, Jiale Chai, and Kazuo Emura. 2025. Application and development of retroreflective Materials: A review. *Energy and Buildings* 337 (2025), 115707. doi:10.1016/j.enbuild.2025.115707

[55] Pengyu Zhang, Dinesh Bharadia, Kiran Joshi, and Sachin Katti. 2016. HitchHike: Practical Backscatter Using Commodity WiFi. In *Proceedings of the 14th ACM Conference on Embedded Network Sensor Systems CD-ROM* (Stanford, CA, USA) *(SenSys '16)*. ACM, New York, NY, USA, 259–271. doi:10.1145/2994551.2994565

[56] Pengyu Zhang, Mohammad Rostami, Pan Hu, and Deepak Ganesan. 2016. Enabling Practical Backscatter Communication for On-Body Sensors. In *Proceedings of the ACM SIGCOMM Conference* (Florianopolis, Brazil) *(SIGCOMM '16)*. ACM, New York, NY, USA, 370–383. doi:10.1145/2934872.2934901

[57] Pengcheng Zhang, Qingxin Yang, Xian Zhang, Yang Li, and Yongjian Li. 2017. Comparative Study of Metal Obstacle Variations in Disturbing Wireless Power Transmission System. *IEEE Transactions on Magnetics* 53, 6 (2017), 1–4. doi:10.1109/TMAG.2017.2657517